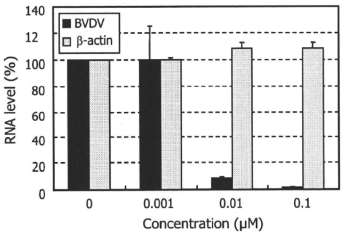

Fig. 3. Effect of SK3M4M5M on BVDV RNA synthesis in MDBK cells. The cells were infected with BVDV at a MOI of 2.0 and cultured in the presence of various concentrations of the compound. After incubation for 12 h, the cells were washed with PBS, treated with lysis buffer and subjected to real-time RT-PCR (see Section 2). Black and gray columns indicate the amounts of BVDV RNA and β-actin RNA, respectively. Data represent means ± SD for triplicate experiments. Experiments were repeated three times, and a representative result is shown.

added during the first 8 h post-infection (Fig. 4A). When the compound was added at a time point later than 8 h after infection, the antiviral activity was lost, and the intracellular viral RNA gradually increased with increasing the time of delayed addition. These results suggest that SK3M4M5M inhibits an event occurring around 8 h after virus infection. Furthermore, an almost identical result was obtained in the experiment with the BVDV RNA polymerase inhibitor BPIP (Fig. 4B). It has been reported that a single cycle of BVDV replication takes 13 h on average and that viral RNA synthesis starts at about 6–8 h after infection (Paeshuyse et al., 2006). Thus, SK3M4M5M appears to interact with a stage in the viral replication cycle that coincides with the onset of viral RNA synthesis.

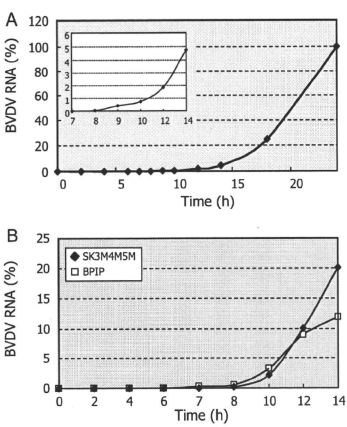

Fig. 4. Effect of time of drug-addition on the antiviral activity of SK3M4M5M. MDBK cells infected with BVDV at a MOI of 2.0. After incubation for 1 h, the inoculum was removed. SK3M4M5M (1 μM) or BPIP (2 μM) was added at the time of infection and incubated without removal of the compound (0 h), or the compound was added at different time points after infection. (A) The cells were further incubated with SK3M4M5M until 24 h after virus infection and subjected to real-time RT-PCR. (B) The cells were further incubated with SK3M4M5 M (filled diamond) or BPIP (open square) up to 24 h after virus infection. Values are expressed as percentage viral RNA of the infected cells untreated with the compound. All data represent means for triplicate experiments. Experiments were repeated twice, and a representative result is shown.

3.3. Activity against NS5B inhibitor-resistant mutants

The antiviral activity of γ-carboline, SK4M5M, SK1M4M5M, and SK3M4M5M was evaluated against three BVDV drug-resistant strains that carry the respective mutations F224S, F224Y, and F291G, which display resistance to BPIP, LZ37, and AG110, respectively. All three molecules have been shown to target the top of the finger domain of the pestivirus RNA polymerase. SK4M5M, and SK1M4M5M, as well as γ-carboline, proved inactive against these mutant strains (Table 2). Interestingly, although SK3M4M5M exhibited reduced activity against the mutant strains, the compound retained overall substantial antiviral activity. Furthermore, the activity of SK3M4M5M against the wild-type of NADL strain was less pronounced than against the Nose strain; however, the anti-BVDV activity was comparable to that of BPIP, which has been reported to be one of the most potent anti-BVDV agents reported so far (Paeshuyse et al., 2006).

3.4. Docking of γ-carboline in the BVDV RNA polymerase crystal structure

The amino acid F224 is located near the tip of the finger domain of the BVDV polymerase. Docking of γ-carboline in this cavity revealed possible interactions between the polymerase and γ-carboline. The following possible interactions were calculated: (i) hydrophobic contacts of γ-carboline with T259, I261 and G223 (Fig. 5A blue shade and Fig. 5B), (ii) a hydrogen bond between the N3 of γ-carboline and the side chain of A392 (Fig. 5A and B), and (iii) aromatic ring stacking interactions between F224 and γ-carboline (Fig. 5A).

3.5. Anti-HCV activity

The γ-carboline derivatives were also examined for their inhibitory effect on HCV replication in replicon cells. However, none of the compounds displayed selective inhibition of HCV replication (data not shown).

4. Discussion

We recently reported two different series of compounds that had selective anti-BVDV activity in cell cultures. One is γ-carboline derivatives, and the other is diphenylmethane derivatives (Sako et al., 2008; Aoyama et al., 2009; Salim et al., 2010). Among them, dimethyl- and trimethyl-γ-carbolines proved to be highly potent and selective inhibitors of BVDV replication (Table 1) (Aoyama et al., 2009). The most potent analogue in this series SK3M4M5M was able to completely inhibit viral RNA synthesis in a single replication cycle assay at a concentration of 100 nM. From a time-of-drug-addition experiment, it appeared that the compound interfered with a step that coincides with the onset of viral RNA synthesis in the replication cycle (Paeshuyse et al., 2009).

Cross-resistance between, two different classes of molecules provides an indirect proof that both have the same molecular target in the viral replication cycle. Therefore, γ-carboline derivatives were examined for their inhibitory effect on the replication of three strains of BVDV that were previously shown to confer resistance to various classes of nonnucleoside NS5B inhibitors (Paeshuyse et al., 2006, 2007, 2009). The antiviral activity of γ-carboline derivatives against the wild-type of NADL strain was several-fold lower than that against the wild-type of Nose strain (Tables 1 and 2). Furthermore, such difference was also observed for their CC_{50} values. This may be attributed to the difference of viral strains and assay conditions used for the experiments, including cytotoxicity evaluation. All of the resistant mutants were less susceptible to the γ-carboline derivatives than the wild-type virus, suggesting that

Table 2
Antiviral activity of γ-carboline derivatives against drug-resistant BVDV in MDBK cells.

Compound	EC_{50} (μM)				CC_{50} (μM)
	WT (NADL strain)	F224S	F224Y	E291G	
γ-Carboline	28.2 ± 9.0	>88.1	>88.1	>88.1	88.1 ± 5.0
SK4M5M	0.38 ± 0.31	>16.7	3.1 ± 0.8	>16.7	16.7 ± 0.7
SK1M4M5M	0.98 ± 0.09	>3.7	>3.7	>3.7	3.7 ± 0.5
SK3M4M5M	0.12 ± 0.06	0.59 ± 0.34	0.58 ± 0.28	0.75 ± 0.34	16.2 ± 1.8
AG110	2.6 ± 1.4	37.8 ± 3.9	30.7 ± 9.0	81.4 ± 6.6	>100
LZ37	12.1 ± 2.6	>92.6	54.7 ± 11.2	6.2 ± 2.0	92.6 ± 5.4
BPIP	0.22 ± 0.02	>76.5	47.8 ± 40.6	1.1 ± 0.1	76.5 ± 2.2

EC_{50}: 50% effective concentration, based on the inhibition of virus-induced cytopathicity; CC_{50}: 50% cytotoxic concentration, based on the reduction of viable cell number. All data represent means ± SD for three independent experiments.

they share the same target with the nonnucleoside NS5B inhibitors AG110, LZ37, and BPIP. The latter compounds were shown to select for drug resistance mutations in the top of the finger domain of the viral polymerase. Interestingly, γ-carboline, SK4M5M, and SK1M4M5M almost completely lost their activity against the resistant mutants. In contrast, SK3M4M5M retained most of its antiviral activity (EC_{50} < 1.0 μM). The methyl group at the 3-position of γ-carboline may possibly play an important role in retaining the antiviral activity against the resistant mutants as well as enhancing the activity against the wild-type strain.

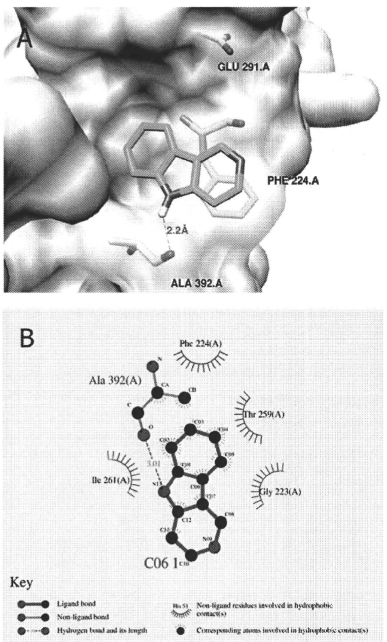

Fig. 5. Modeling of γ-carboline near the position of F224 in BVDV RNA-dependent RNA polymerase. (A) Overview of the entire structure of the RNA polymerase with γ-carboline docked in the vicinity of F224. Picture generated using UCSF Chimera (Pettersen et al., 2004). (B) Ligplot depicting a simplified representation of interactions between γ-carboline and the RNA polymerase. Carbon atoms are black, nitrogen atoms are blue, and oxygen atoms are red. A putative hydrogen bond is drawn as a dotted black line in panel A and a dotted green line in panel B. Spiked red line indicates the hydrophobic interactions.

We hypothesize that the apparent lack of cross-resistance of SK3M4M5M with the drug resistant strains can be explained by a different binding mode of each analogue, as compared to that of γ-carboline; likely due to the different degree of methylation and the position of the methyl groups. For SK3M4M5M, the methyl group in position 3 is optimal to interact with the wild-type RNA polymerase. However, this methyl group will shift the interaction of the molecule, as compared to γ-carboline. Most probably, this shift will result in the loss of the aromatic ring stacking interaction between F224 or Y224 and γ-carboline. Hence, the effect on compound activity may be reduced, when these residues are mutated to non-aromatic residues in the drug-resistant strains.

BVDV is considered to be a valuable surrogate virus for identifying and characterizing anti-HCV compounds. BVDV shares many characteristic similarities with HCV in virion structure, genome organization, and replication machinery (Buckwold et al., 2003; Nam et al., 2001). However, it is not surprising that SK3M4M5M did not have selective anti-HCV activity in HCV RNA replicon cells. A possible explanation is the difference between BVDV NS5B and HCV NS5B molecules. It was recently reported that BPIP, which is inactive against HCV, became active, when one or two fluorine molecules were introduced into certain positions of this compound (Vliegen et al., 2009). Currently, this approach has not been successful for γ-carboline derivatives (data not shown).

In conclusion, our results clearly demonstrate that novel γ-carboline derivatives, especially, 3,4,5-trimethyl-γ-carboline (SK3M4M5M) is a highly potent and selective inhibitor of BVDV replication in cell cultures. Although further studies, such as selection of drug-resistant mutants and inhibition of in vitro transcription, are required, the compound may target NS5B RNA polymerase. It retains sufficient activity against the mutant viruses that are resistant to already known nonnucleoside NS5B inhibitors. Thus, this class of compounds should be further pursued for their use in the field of veterinary medicine.

Acknowledgments

This work was in part supported by the Science and Technology Incubation Program in Advanced Regions, Japan Science and Technology Agency (JST), Japan. We thank the Egyptian Government for support to M.T.A. Salim, who was previously an assistant lecturer in the Faculty of Pharmacy, Al-Azhar University, Egypt and is currently a postgraduate student of Kagoshima University, Japan.

References

Aoyama, H., Sako, K., Sato, S., Nakamura, M., Miyachi, H., Goto, Y., Olamoto, M., Baba, M., Hashimoto, Y., 2009. Polymethylated γ-carbolines with potent anti-bovine viral diarrhea virus (BVDV) activity. Heterocycles 77, 779–785.

Baba, C., Yanagida, K., Kanzaki, T., Baba, M., 2005. Colorimetric lactate dehydrogenase (LDH) assay for evaluation of antiviral activity against bovine viral diarrhea virus (BVDV) in vitro. Antiviral Chem. Chemother. 16, 33–39.

Baginski, S.G., Pevear, D.C., Seipel, M., Sun, S.C., Benetatos, C.A., Chunduru, S.K., Rice, C.M., Collett, M.S., 2000. Mechanism of action of a pestivirus antiviral compound. Proc. Natl. Acad. Sci. U.S.A. 97, 7981–7986.

Buckwold, V.E., Beer, B.E., Donis, R.O., 2003. Bovine viral diarrhea virus as a surrogate model of hepatitis C virus for the evaluation of antiviral agents. Antiviral Res. 60, 1–15.

Chang, J., Wang, L., Ma, D., Qu, X., Guo, H., Xu, X., Mason, P.M., Bourne, N., Moriarty, R., Gu, B., Guo, J.T., Block, T.M., 2009. Novel imino sugar derivatives demonstrate potent antiviral activity against flaviviruses. Antimicrob. Agents Chemother. 53, 1501–1508.

Choi, K.H., Groarke, J.M., Young, D.C., Kuhn, R.J., Smith, J.L., Pevear, D.C., Rossmann, M.G., 2004. The structure of the RNA-dependent RNA polymerase from bovine viral diarrhea virus establishes the role of GTP in de novo initiation. Proc. Natl. Acad. Sci. U.S.A. 101, 4425–4430.

Houe, H., 2003. Economic impact of BVDV infection in dairies. Biologicals 31, 137–143.

Ishii, N., Watashi, K., Hishiki, T., Goto, K., Inoue, D., Hijikata, M., Wakita, T., Kato, N., Shimotohno, K., 2006. Diverse effects of cyclosporine on hepatitis C virus strain replication. J. Virol. 80, 4510–4520.

Kalaycioglu, A.T., 2007. Bovine viral diarrhoea virus (BVDV) diversity and vaccination. A review. Vet. Q. 29, 60–67.

Kobrak, A., Weber, E.L., 1997. Bovine diarrhea virus: an update. Rev. Argent. Microbiol. 29, 47–61.

Luscombe, C.A., Huang, Z., Murray, M.G., Miller, M., Wilkinson, J., Ewart, G.D., 2010. A novel Hepatitis C virus p7 ion channel inhibitor BIT225, inhibits bovine viral diarrhea virus in vitro and shows synergism with recombinant interferon-α-2b and nucleoside analogues. Antiviral Res. 86, 144–153.

Mohamadi, F., Richards, N.G.J., Guida, W.C., Liskamp, R., Lipton, M., Caufield, C., Chang, C., Hendrickson, T., Still, W.C., 1990. An integrated software system for modeling organic and bioorganic molecules using molecular mechanics. J. Comput. Chem. 11, 440–467.

Morris, G.M., Goodsell, D.S., Halliday, R.S., Huey, R., Hart, W.E., Belew, R.K., Olsen, A.J., 1998. Automated docking using a Lamarckian genetic algorithm and empirical binding free energy function. J. Comput. Chem. 19, 1639–1662.

Nam, J.H., Bukh, J., Purcell, R.H., Emerson, S.U., 2001. High-level expression of hepatitis C virus (HCV) structural proteins by a chimeric HCV/BVDV genome propagated as a BVDV pseudotype. J. Virol. Methods 97, 113–123.

Okamoto, M., Sakai, M., Goto, Y., Salim, M.T.A., Baba, C., Goto, K., Watashi, K., Shimotohno, K., Baba, M., 2009. Anti-bovine viral diarrhea virus and hepatitis C virus activity of the cyclooxygenase inhibitor SC-560. Antiviral Chem. Chemother. 20, 47–54.

Paeshuyse, J., Leyssen, P., Mabery, E., Boddeker, N., Vrancken, R., Froeyen, M., Ansari, I.H., Dutartre, H., Rozenski, J., Gil, L.H., Letellier, C., Lanford, R., Canard, B., Koenen, F., Kerkhofs, P., Donis, R.O., Herdewijn, P., Watson, J., De Clercq, E., Puerstinger, G., Neyts, J., 2006. A novel, highly selective inhibitor of pestivirus replication that targets the viral RNA-dependent RNA polymerase. J. Virol. 80, 149–160.

Paeshuyse, J., Chezal, J.M., Froeyen, M., Leyssen, P., Dutartre, H., Vrancken, R., Canard, B., Letellier, C., Li, T., Mittendorfer, H., Koenen, F., Kerkhofs, P., De Clercq, E., Herdewijn, P., Puerstinger, G., Gueiffier, A., Chavignon, O., Teulade, J.C., Neyts, J., 2007. The imidazopyrrolopyridine analogue AG110 is a novel, highly selective inhibitor of pestiviruses that targets the viral RNA-dependent RNA polymerase at a hot spot for inhibition of viral replication. J. Virol. 81, 11046–11053.

Paeshuyse, J., Letellier, C., Froeyen, M., Dutartre, H., Vrancken, R., Canard, B., De Clercq, E., Gueiffier, A., Teulade, J.C., Herdewijn, P., Puerstinger, G., Koenen, F., Kerkhofs, P., Baraldi, P.G., Neyts, J., 2009. A pyrazolotriazolopyrimidinamine inhibitor of bovine viral diarrhea virus replication that targets the viral RNA-dependent RNA polymerase. Antiviral Res. 82, 141–147.

Pettersen, E.F., Goddard, T.D., Huang, C.C., Couch, G.S., Greenblatt, D.M., Meng, E.C., Ferrin, T.E., 2004. UCSF chimera - a visualization system for exploratory research and analysis. J. Comput. Chem. 25, 1605–1612.

Sako, K., Aoyama, H., Sato, S., Hashimoto, Y., Baba, M., 2008. γ-Carboline derivatives with anti-bovine viral diarrhea virus (BVDV) activity. Bioorg. Med. Chem. 16, 3780–3790.

Salim, M.T.A., Okamoto, M., Hosoda, S., Aoyama, H., Hashimoto, Y., Baba, M., 2010. Anti-bovine viral diarrhea virus activity of novel diphenylmethane derivatives. Antiviral Chem. Chemother. 20, 193–200.

Schuettelkopf, A.W., van Aalten, D.M.F., 2010. PRODRG - a tool for high-throughput crystallography of protein–ligand complexes. Acta Crystallogr. D60, 1355–1363.

Tabarrini, O., Manfroni, G., Fravolini, A., Cecchetti, V., Sabatini, S., De Clercq, E., Rozenski, J., Canard, B., Dutartre, H., Paeshuyse, J., Neyts, J., 2006. Synthesis and anti-BVDV activity of acridones as new potential antiviral agents. J. Med. Chem. 49, 2621–2627.

van Oirschot, J.T., Bruschke, C.J., van Rijn, P.A., 1999. Vaccination of cattle against bovine viral diarrhoea. Vet. Microbiol. 64, 169–183.

Vliegen, I., Paeshuyse, J., De Burghgraeve, T., Lehman, L.S., Paulson, M., Shih, I.H., Mabery, E., Boddeker, N., De Clercq, E., Reiser, H., Oare, D., Lee, W.A., Zhong, W., Bondy, S., Pürstinger, G., Neyts, J., 2009. Substituted imidazopyridines as potent inhibitors of HCV replication. J. Hepatol. 50, 999–1009.

Watashi, K., Hijikata, M., Hosaka, M., Yamaji, M., Shimotohno, K., 2003. Cyclosporine A suppresses replication of hepatitis C virus genome in cultured hepatocytes. Hepatology 38, 1282–1288.

Wallace, A.C., Laskowski, R.A., Thornton, J.M., 1995. LIGPLOT: a program to generate schematic diagrams of protein–ligand interactions. Prot. Eng. 8, 127–134.

Yanagida, K., Baba, C., Baba, M., 2004. Inhibition of bovine viral diarrhea virus (BVDV) by mizoribine: synergistic effect of combination with interferon-α. Antiviral Res. 64, 195–201.

Langmuir
Article
pubs.acs.org/Langmuir

A New Optical Label-Free Biosensing Platform Based on a Metal−Insulator−Metal Structure

Amir Syahir,[†] Hisakazu Mihara,[†] and Kotaro Kajikawa*[,‡]

[†]*Graduate School of Bioscience and Biotechnology, Tokyo Institute of Technology, Yokohama 226-8501, Japan, and* [‡]*Interdisciplinary Graduate School of Science and Engineering, Tokyo Institute of Technology, Yokohama 226-8502, Japan*

Received October 7, 2009. Revised Manuscript Received February 1, 2010

A new label-free biosensing platform is proposed based on a metal−insulator−metal (MIM) structure. This platform allows us to perform biosensing by a simple reflectivity measurement at normal incidence illumination without using any bulky optical setup. Theoretical calculation was made to find optimized MIM structural parameters, and experimental results on the label-free biosensing using the MIM platform are presented. This platform has greater sensitivity and mass resolution with respect to the anomalous reflection method, which is a label-free biosensing platform previously proposed by us. Hence, it is suitable for high throughput analysis of biomolecular detection in a microarray format.

Introduction

As a label-free optical sensor for probing the biomolecular interaction, surface plasmon resonance (SPR) spectroscopy has been widely used using the attenuated total reflection (ATR) geometry.[1−3] Since the dispersion relation of surface plasmons (SPs) in a metal differs from that of light propagating in free space, the SPR condition is usually achieved in the ATR geometry using prism-coupling optics with oblique incidence excitation. This is not convenient for multichannel SPR imaging or portable miniaturized sensing systems. Localized surface plasmon resonance (LPR) in metallic nanostructures is another label-free biosensing platform, which works without using any bulky optical setup.[4−6] This platform is compatible with miniaturized sensors, since the LPR condition can be achieved at normal-incidence excitation. However, performance of the LPR sensing critically depends on the surface nanostructures, so that the precise control of the surface nanostructures is necessary to make quantitative analysis.

Anomalous reflection (AR) at a gold surface, we recently proposed, is another label-free optical biosensing platform applicable to detection of various biomolecular interactions.[7−11] This method is an application of the phenomenon that the reflectivity at gold surface for blue or purple light (λ = 400−480 nm) is reduced upon adsorption of a thin dielectric film. AR can be achieved by normal-incidence illumination and has a good theoretical spatial resolution of less than 1 μm.[11] Therefore, it is a potential platform for a simple and practical label-free multichannel biochips. However, sensitivity of the AR biosensing is an order of magnitude less than that of the ATR-based SPR.

Meanwhile, metal−insulator−metal (MIM) structures have been used for various purposes, especially in electronic[12−15] and optoelectronic[16−19] fields. As for the surface plasmon effect in MIM structures,[16−21] it has been shown that by changing the thickness of the sandwiched insulator layer, one can control surface plasmons excited in the MIM waveguides. The MIM surface plasmons can be excited with propagating light without using ATR geometry.[16] Hence, unlike the ATR-based SPR, the SPR condition can be achieved in a simple reflection geometry even at normal incidence. Such properties have been applied to enhancement of photoemission from the insulator layer.[19−21] Nevertheless, the MIM-based optical biosensor has yet to be explored.

Recently, our optical reflectivity calculation revealed that the AR effect is enhanced if we use a MIM structure (Figure 1a) as an AR substrate. The enhancement comes from the fact that the apparent complex dielectric constant of the MIM substrate produces optimum phase of the complex reflection coefficient at the surface, resulting in a large reflectivity change upon adsorption of a thin dielectric film. The modified phase can be attributed to the MIM surface plasmon effect. This mechanism is reported in our previous paper (Appendix of ref 11). The apparent reflectivity is obtained by a usual manner using the transfer matrix method.[22] Herein, we report the theoretical and experimental results of the MIM-enhanced AR biosensing (MIM biosensing).

*Corresponding author: Tel +81-45-924-5596; e-mail kajikawa@ep.titech.ac.jp.

(1) Knoll, W. *Annu. Rev. Phys. Chem.* **1993**, *49*, 569–633.
(2) Homola, J.; Yee, S. S.; Gauglitz, G. *Sens. Actuators, B* **1999**, *54*, 3–15.
(3) Homola, J. *Chem. Rev.* **2008**, *108*, 462–493.
(4) Nath, N.; Chilkoti, A. *Anal. Chem.* **2004**, *76*, 5370–5378.
(5) Haes, A. J.; Van Duyne, R. P. *J. Am. Chem. Soc.* **2002**, *124*, 10596–10604.
(6) Mitsui, K.; Handa, Y.; Kajikawa, K. *Appl. Phys. Lett.* **2004**, *85*, 4231–4233.
(7) Watanabe, M.; Kajikawa, K. *Sens. Actuators, B* **2003**, *86*, 126–130.
(8) Watanabe, S.; Usui, K.; Tomizaki, K.-Y.; Kajikawa, K.; Mihara, H. *Mol. BioSyst.* **2005**, *1*, 363–365.
(9) Watanabe, S.; Tomizaki, K.-Y.; Takahashi, T.; Usui, K.; Kajikawa, K.; Mihara, H. *Biopolymers* **2007**, *88*, 131–140.
(10) Syahir, A.; Tomizaki, K.-Y.; Kajikawa, K.; Mihara, H. *Langmuir* **2009**, *25*, 3667–3674.
(11) Fukuba, S.; Naraoka, R.; Tsuboi, K.; Kajikawa, K. *Opt. Commun.* **2009**, *282*, 3386–3391.
(12) Waser, R.; Aono, M. *Nat. Mater.* **2007**, *6*, 833–840.
(13) Yang, J. J.; Pickett, M. D.; Li, X.; Ohlberg, D. A. A.; Stewart, D. R.; Williams, R. S. *Nat. Nanotechnol.* **2008**, *3*, 429–433.
(14) Maisch, S.; Buckel, F.; Effenberger, F. *J. Am. Chem. Soc.* **2005**, *127*, 17315–17322.
(15) Loo, Y.-L.; Willet, R. L.; Baldwin, K. W.; Rogers, J. A. *J. Am. Chem. Soc.* **2002**, *124*, 7654–7655.
(16) Economou, E. N. *Phys. Rev.* **1969**, *182*, 539–554.
(17) Engheta, N. *Science* **2007**, *317*, 1698–1702.
(18) Hosseini, A.; Massoud, Y. *J. Opt. Soc. Am. A* **2007**, *24*, 221–224.
(19) Lei, D. Y.; Ong, H. C. *Appl. Phys. Lett.* **2006**, *91*, 211107.
(20) Liu, J. S. Q.; Brongersma, M. L. *Appl. Phys. Lett.* **2007**, *90*, 091116.
(21) Feng, J.; Okamoto, T.; Simonen, J.; Kawata, S. *Appl. Phys. Lett.* **2007**, *90*, 081106.
(22) Bethune, D. S. *J. Opt. Soc. Am. B* **1989**, *6*, 910–916.

 Published on Web 02/16/2010 **DOI:** 10.1021/la903794b

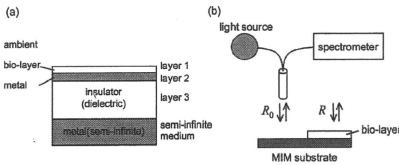

Figure 1. (a) Schematic drawing of metal−insulator−metal (MIM) structure for biosensing application. Layer 1 is considered to be a detected biolayer. An insulator film (layer 3) is sandwiched with two gold media. (b) Optical setup for reflectivity measurement. Reflectivity in the absence of layer 1. R_0, is taken as reference.

The theoretical calculation showed severalfold enhancement of sensitivity with respect to the conventional AR method. Several conditions for the MIM biosensing were experimentally tested, and the results are shown to be agreeable to the theoretical calculations. The MIM platform has a few advantages over the ATR-based SPR: (1) It is achieved with simple optical setup because of the simple reflectivity measurement at normal incidence. (2) It has a good spatial resolution because light do not propagate along the surface, while ATR-based SPR has a spatial resolution of tens of micrometers originating from long propagation length of surface plasmons.[23] This is because the surface plasmons excited in MIM structures at normal incidence illumination do not propagate along the surface, in principle, since the illumination light has no in-plane component of the wave vector. This feature allows us to use the MIM-biosensing platform to fabricate a high-density multichannel biochips, similarly to the high-density protein AR biochips we previously reported.[11] (3) It has a tolerance for angle of incidence and excitation wavelength. This allows us to use an incoherent light source such as a light-emitting diode (LED).

Experiment

Chemicals and Reagents. 1-Amino-8-octancethiol (AOT), dithiobis(succinimidyl undecanoate), and sulfosuccinimidyl-D-biotin (biotin-OSu) were purchased from Dojindo, Japan. Forth generation poly(amidoamine)dendrimer (PAMAM-G4) and avidin (egg white) were purchased from Sigma-Aldrich. All solvents used were purchased from Kanto Chemical, Japan. These chemicals were used as received. Water was purified with a Milli-Q production system. For the buffer solution, phosphate-buffered saline, PBS (10 mM phosphate, 150 mM NaCl, pH 7.4), was used.

Fabrication of Au−PMMA−Au MIM Thin Films and Biotin Modification. A thin gold film 150 nm thick was vacuum-evaporated on a silica slide at a pressure of 10^{-5} Pa using a heat-evaporation machine equipped with a QCM device (parallel with the silica slide). This film was used as a semi-infinite medium. A thin film of poly(methyl methacrylate) (PMMA) was used as an insulator layer (layer 3), which was spin-coated on the gold-covered silica slide at 6000 rpm in 1 min with different concentration. The concentrations used were 1.0, 1.7, 2.3, 3.0, and 4.0 wt % of PMMA in 2-ethoxyethyl acetate to produced thin layer at approximately 15, 30, 40, 55, and 80 nm in thickness, respectively. The thickness was determined by fitting the reflectivity spectrum to the theoretically calculated one. After deposition of the PMMA film, the top layer of gold (layer 2) was vacuum-evaporated at the same condition in the thickness of 5, 10, 15, and 20 nm. Then, substrate was immersed in an ethanolic solution of AOT (SAM) at a 0.1 mM for 30 min at room temperature. After washing the AOT-modified substrate with ethanol, the substrate was dried with a stream of air. After that, the substrate was reacted with 0.1 mM biotin-OSu in water for 30 min, rinsed with water, and dried with a stream of air. With the biotin-modified substrates, we assayed avidin solutions and the measurements were made in air (dry) or in water.

Table 1. Parameters Used in the Calculation of R_0 and R_1 for Figure 2b[a]

	material	dielectric constant	thickness (nm)
ambient	air	1.0	
layer 1	biomolecules	2.25	1.0
layer 2	gold	ε_{Au}	10
layer 3	PMMA	2.25	d_3
semi-infinite layer	gold	ε_{Au}	

[a] The dielectric constant of gold, ε_{Au}, in the literature[24] was used.

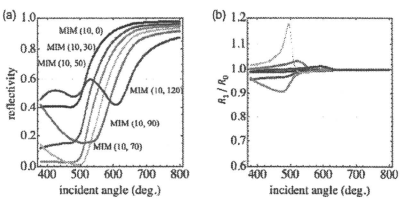

Figure 2. (a) Calculated spectra of reflectivity of MIM substrates without layer 1. (b) Normalized reflectivity, R_1/R_0, upon formation of a 1 nm thick dielectric layer with a dielectric constant of 2.25.

Reflectivity Measurement. The reflection absorption (RA) spectroscopy was made with a multichannel spectrometer (MCPD-3000, Otsuka Electronics Ltd., Japan). As shown in Figure 1b, the light from a halogen lamp (PHL-150, Sigma Koki, Japan) was guided to the sample surface by a Y-type optical fiber and was illuminated at normal incidence. The reflected light was brought to the spectrometer via the optical fiber. The typical exposure time was about 200 ms, and the number of runs for accumulation was 30 times.

Results and Discussion

The MIM structure used in this study is depicted in Figure 1a. An insulator film (layer 3) is sandwiched by a thin gold film (layer 2) and a semi-infinite medium of gold to form an MIM structure. The 150 nm thick gold film is thick enough to be considered as semi-infinite. As for layer 2 (top Au thinlayer), we regard a vacuum-evaporated 10 nm thick Au layer to be almost continuous. The biosensing process, binding of analyte to ligand, can be considered as an increase in thickness of layer 1. The reflectivity in the absence of layer 1, R_0, and the reflectivity in the presence of 1 nm thickness of layer 1, R_1, are calculated using the transfer matrix technique[22] with the parameters tabulated in Table 1. The dielectric constant from a literature was used.[24] Figure 2a,b plots the calculated spectra of R_0 and R_1/R_0 at $d_2 = 10$ nm and $d_3 = 0$, 30, 50, 70, 90, and 120 nm, where d_i stands for the thickness of layer i. From now on, we abbreviate the MIM structures having thicknesses (d_2, d_3) to MIM (d_2, d_3). The sample of $d_3 = 0$ is equal to a gold film, corresponding to the AR platform. One may see in Figure 2b that deposition of a 1 nm thick dielectric film (layer 1) results in the greatest difference in

(23) Lamprech, B.; Krenn, J. R.; Schider, G.; Ditlbacher, H.; Salerno, M.; Felidj, N.; Leitner, A.; Aussenegg, F. R. *Appl. Phys. Lett.* **2001**, *79*, 51–53.

(24) Johnson, P. B.; Christy, R. W. *Phys. Rev. B* **1972**, *6*, 4370–4379.

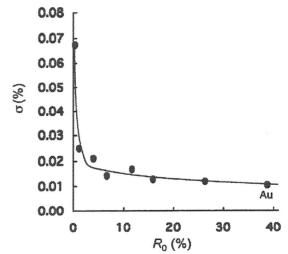

Figure 3. Standard deviation, σ of the 10 R_0 values measured for 1 s. Experiment were conducted with seven different MIM substrates; from left is MIM (5, 55), MIM (10, 55), MIM (5, 40), MIM (10, 40), MIM (15, 40), MIM (10, 30), MIM (10, 15), and MIM (0, 0) substrate (control) which possess R_0 value ranging from 0.4 to 38.8% at their sensitive wavelength.

reflectivity (19%) at $d_3 = 70$ nm. This is as much as ca. 15 times larger than the previously reported AR values. However, the MIM structures having such a large sensitivity are difficult for practical use. In addition, the wavelength range of MIM (10, 70) for sensing is rather narrow, resulting in serious control of the insulator layer thickness. This is because such samples have small R_0 (less than 1%) at the sensitive wavelengths (λ = 500 nm), which bring about bad signal-to-noise ratios. To show this, we experimentally examined the relation between R_0 and the error, by evaluating the standard deviation, σ, of the 10 R_0 values measured for 1 s. We had chosen seven different MIM substrates of MIM (5, 55), MIM (10, 55), MIM (5, 40), MIM (10, 40), MIM (15, 40), MIM (10, 30), MIM (10, 15), and MIM (0, 0) which possess R_0 value ranging from 0.4 to 38.8% at their sensitive wavelength (deepest absorbance of each substrate). The results are plotted in Figure 3. It was confirmed that the standard deviation scarcely changed if we increase the number of the measurements up to 60. The error was less than 0.025% for $R_0 > 1.0\%$, and it is much larger for $R_0 < 1.0\%$. The σ value involves many causes of error, such as an instrument resolution, fluctuation of the light source intensity, and electrical noise. Hence, the geometries having $R_0 < 1.0\%$ are excluded in our consideration.

Furthermore, to find the optimized condition, we calculated the R_0 and R_1/R_0 profiles in air with other thickness parameters of d_2 and d_3 (see Supporting Information). The calculated R_0, sensitivity, s, and mass resolution, σ_m, for $d_2 = 10$ and 15 nm are summarized in Table 2. The sensitivity is defined as a decreasing rate in reflectivity with respect to R_0 upon adsorption of layer 1 (1 nm thick and dielectric constant of 2.25), namely $s = 1 - R_1/R_0$. The mass resolution is calculated by $\sigma_m = \sigma/s$,[25,26] assuming unity mass density of layer 1. The density of layer 1 was assumed to be 1 g/cm^3 for calculation convenience.[11] The mass resolution of analyte with density ξ can be evaluated by multiplying the ξ value to σ/s. Typical ξ for protein is $\xi = 1.2-1.4$. The σ values were estimated from Figure 3. There are many MIM structures that show good mass resolution (see Supporting Information for $d_2 = 5$ and 20 nm). However, samples with $d_2 = 5$ nm is practically unsuitable to the MIM-biosensing platform because a thin gold films less than 5 nm thick is usually discontinuous and forming island structures. Although the calculated sensitivity is considerably large for MIM (15, 70) and MIM (20, 90), they are excluded because of low reflectivity ($R_0 < 1\%$). Among calculated samples, we conclude that MIM (10, 50) having $s = 9.5\%$ nm^{-1} and $\sigma_m = 2.6$ pg mm^{-2} is the most suitable for the sensing in air, considering both the structure of the continuous thin gold film and its relatively high R_0.

Table 2. Theoretical Reflectivity R_0, Calculated Sensitivity s, Measured Error σ, and Estimated Mass Resolution σ_μ of MIM Substrate at Their Sensitive Wavelength λ in Air

d_2 (nm)	d_3 (nm)	R_0 (%)	s (% nm^{-1})	σ (%)	σ_μ (pg mm^{-2})	λ (nm)
0[a]	0	40	1.2	0.011	9.1	470
10[a]	30	15	3.5	0.013	3.7	470
10[a]	40	7.0	5.0	0.016	3.2	470
10	50	3.0	9.5	0.025	2.6	470
10[a]	55	1.1	14	0.05	3.6	470
10	70	1.0	19	0.05	2.6	500
10	90	15	3.0	0.013	4.3	520
10	120	45	1.0	0.011	11	600
15	30	18	2.5	0.013	5.2	470
15[a]	40	10	3.8	0.015	4.0	470
15	50	6.0	5.5	0.018	3.0	490
15	70	0.1	25			505
15	90	3.5	7.5	0.03	4.0	520
15	120	20	2.0	0.012	6.0	590

[a] Substrates experimentally tested in this study.

Table 3. Theoretical Reflectivity R_0, Calculated Sensitivity s, Measured Error σ, and Calculated Mass Resolution σ_m of MIM Substrate at Their Sensitive Wavelength λ in Water

d_2 (nm)	d_3 (nm)	R_0 (%)	s (% nm^{-1})	σ (%)	σ_m (pg mm^{-2})	λ (nm)
0[a]	0	35	0.6	0.012	20	470
10	30	10	1.5	0.015	10	400
10	50	3.0	2.5	0.025	10	450
10	70	0.8	−5.0	0.055	11	470
10[a]	80	4.2	−2.2	0.017	8.0	470
10	90	10	−1.0	0.015	15	470
10	120	40	0.2	0.011	55	470
15	30	15	1.5	0.013	8.6	470
15[a]	40	8.0	1.8	0.016	9.0	470
15	50	4	2.5	0.017	6.8	470
15[a]	55	2.2	3.0	0.025	8.0	470
15	70	0	4.0			490
15[a]	80	1.0	4.5	0.05	11	500
15	90	5	1.8	0.02	11	505
15	120	27	0.5	0.012	24	580

[a] Substrates experimentally tested in this study.

Table 3 summarizes the calculated results for ambient of water for $d_2 = 10$ and 15 nm (see Supporting Information for $d_2 = 5$ and 20 nm). The mass resolutions are a few times worse than those listed in Table 2 (in air) due to smaller difference between refractive index of water (1.33) and biomolecular layer (ca. 1.5), resulting in less sensitivity to the biosensing process. From all calculated samples in water, we conclude that MIM (10, 70) having $s = 6.0\%$ nm^{-1} and $\sigma_m = 9.2$ pg mm^{-2} is the most suitable for the sensing.

The measurement of MIM (0, 0) corresponds to the AR detection. In Table 2, MIM (0, 0) has a resolution of $\sigma_m = 9.1$ pg mm^{-2}, which is much better than the previously reported value, $\sigma_m = 40$ pg mm^{-2}.[11] This is because of the difference in the optical setup: this study adopts a low noise spectrometer using a photodiode-array detector. In the case of water ambient, σ_m = 20 pg mm^{-2} for the AR detection.

For comparison, we calculated mass resolutions in the ATR-based SPR measurements at a wavelength of 633 nm. The considered model for ambient of air is composed of a rectangular

(25) Nelson, S. G.; Johnston, K. S.; Yee, S. S. *Sens. Actuators, B* **1996**, *35−36*, 187−191.
(26) Naraoka, R.; Kajikawa, K. *Sens. Actuators, B* **2005**, *107*, 952−956.

Table 4. Reflectivity R_0, Calculated Sensitivity s, Measured Error σ, and Calculated Mass Resolution σ_m at Angle of Incidence θ_{nr} of ATR-Based SPR Measurements at λ = 633 nm

ambient	θ_{nr} (deg)	R_0 (%)	s (% nm^{-1})	σ (%)	σ_m (pg mm^{-2})
air	44.2	5.0	160	0.02	0.13
water	57.2	5.0	60	0.02	0.33

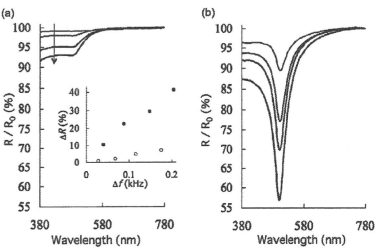

Figure 4. (a) Normalized reflectivity spectra of the MIM (0, 0) substrate upon formation of MgF_2 thin layers stepwisely evaporated; (b) those of MIM(20, 70). Inset of (a) shows ΔR of MIM(0, 0) (open circle) and that of MIM(20, 70) (filled circle) as a function of QCM frequency change (Δf).

prism (refractive index 1.5) with a 47 nm thick thin gold film (a refractive index of $(-10.8 + 1.47i)^{1/2}$) at the bottom. A high index rectangular prism (a refractive index of 1.85) was considered for ambient of water (refractive index of 1.33). The calculation was made at the near resonance angle θ_{nr} that gives R_0 = 5%. We examined the standard deviation in the ATR-based SPR measurements and found to be 0.02%. The results are summarized in Table 4. The mass resolutions σ_m in the ATR-based SPR measurements are 0.13 pg mm^{-2} for air ambient and 0.33 pg mm^{-2} for water ambient, which are an order of magnitude better than those of the MIM biosensing platform.

Experiments were made to confirm the theoretical calculation of MIM biosensing based on the transfer matrix technique.[22] They were carried out with MIM (20, 70) by deposition of thermally evaporated MgF_2 thin films on the MIM surface (Figure 4b). For reference, the AR-based measurement was also made using the sample MIM(0, 0) (Figure 4a). The inset of Figure 4a shows the relation between the rate of decrease in reflectivity, $\Delta R = 1 - R/R_0$, at λ = 500 nm and the changes in the quartz microbalance (QCM) frequency, Δf. The QCM device was equipped in the vacuumed evaporation chamber. Experimentally acquired reflectivity of the MIM structure is defined as R, where the surface is covered with layer 1. A MgF_2 film has a refractive index of 1.38, which is lower than that of biomolecular films, resulting in the lower theoretical AR sensitivity s = 0.90% nm^{-1}. From the slope of the AR profile, we can determine the thickness of the MgF_2 thin films from the ΔR–Δf profile (open circle in the inset of Figure 4a). We found the sensitivity of the MIM structure s = 4.7% nm^{-1} from the inset of Figure 4a (closed circle). This value is close to the theoretically calculated rate of s = 5.0% nm^{-1}, assuming a layer 1 with a refractive index 1.38, using the transfer matrix technique.[22]

Moreover, we assayed a 100 nM protein (avidin) solution in PBS buffer onto biotin-modified MIM substrates. As an exemplar, we selected some MIM samples: MIM (10, 30), MIM (10, 40), MIM (10, 55), MIM (15, 40), and a control of MIM (0, 0). We excluded MIM(10, 70) having good sensitivity in

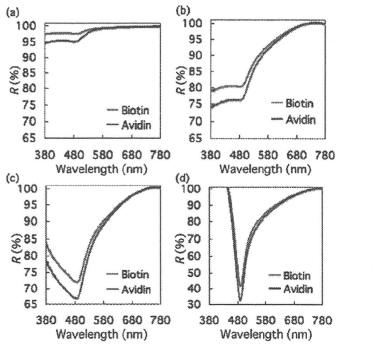

Figure 5. Molecular interactions (biotin–avidin) detected using (a) MIM (0, 0), (b) MIM (10, 30), (c) MIM (10, 40), and (d) MIM (10, 55) substrates.

Table 5. ΔR for Binding of Avidin to Biotinylated Substrates in Air and Evaluated Thickness, d_1

d_2 (nm)	d_3 (nm)	ΔR (%)	s (% nm^{-1})	d_1 (nm)
0	0	2.0	1.2	1.7
10	30	4.2	3.5	1.2
10	40	5.3	5.0	1.1
10	55	9.2	14	0.66
15	40	4.9	3.8	1.3

Table 2, since the allowable margin of the insulator layer thickness is narrow. The reflectivity measurements were made in air after rinse and a drying process as previously shown.[10] The spectra before and after avidin binding event are also shown in Figure 5. The results of the change rates of reflectivity, ΔR, for binding of avidin to biotinylated substrates are summarized in Table 5. As shown in the table, the ΔR upon interactions of avidin with surface bound biotin is listed along with calculated sensitivity, s, of each substrate. Then, the avidin thickness, d_1 (nm), is evaluated using the approximation $d_1 = \Delta R/s$. From those tested MIM samples, MIM (10, 40) and MIM (10, 55) show signal (ΔR) improvement of 2.7- and 4.6-fold, respectively, in comparison with MIM (0, 0) substrate. The evaluated avidin thicknesses, d_1, for MIM (10, 30), MIM (10, 40), and MIM (15, 40) ranging from 1.1 to 1.3 nm are almost in agreement for MIM samples with the exception of 0.24 nm for MIM (10, 55). The exceptionally small d_1 evaluated with MIM (10, 55) is due to saturation of ΔR. In Figure 5d, the biotinylated substrate of MIM (10, 55) has large ΔR, resulting in small ΔR upon the binding avidin event. The d_1 values are somewhat smaller than the reported ones[1,27,28] because the low concentration of the avidin solution produces in the partially covered layer. To enhance surface coverage of captured protein on the MIM platform, we implement surface chemistry modification with PAMAM-G4.[10] When comparing the ΔR of avidin on MIM (10, 55) with PAMAM-G4 modification (Figure 6) and without the modification (Figure 5d), we observed an additional enhancement of 2.6-fold. Concentration

(27) Misawa, N.; Yamamura, S.; Kim, Y.-H.; Tero, R.; Nonogaki, Y.; Urisu, T. *Chem. Phys. Lett.* **2006**, *419*, 86–90.
(28) Ebersole, R. C.; Miller, J. A.; Moran, J. R.; Ward, M. D. *J. Am. Chem. Soc.* **1990**, *112*, 3239–3241.

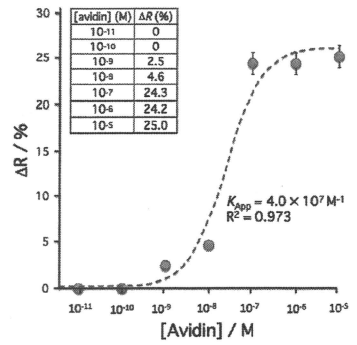

Figure 6. Adsorption profiles for avidin onto biotinylated PAMAM G4-modified MIM (10, 55) substrate measured in air. Plots were fitted with the Langmuir adsorption isotherm equation. Inset were data plotted.

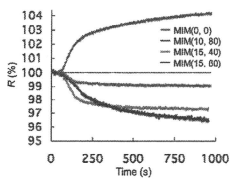

Figure 7. *In-situ* measurement of biotin–avidin interactions in 200 μL cell. Protein was injected at ~100 s.

dependency of interactions between avidin and surface-bound biotin (Figure 6) shows an apparent affinity constant, K_{App} = 4.0×10^7 M^{-1}, which is comparable to those reported in literature[29–33] ($K_{App} = 10^6 - 10^8$ M^{-1}, depending on type of surface and biosensor applied therein), indicating the adequacy of MIM-based biosensor.

Finally, we show the binding process of avidin to a biotinylated substrate in PBS buffer (Figure 7). The substrates MIM (0, 0), MIM (10, 80), MIM (15, 40), and MIM (15, 80) were used. Exposure of the biotinylated substrate to avidin results in the change in the reflectivity, ΔR, with time t, while ΔR rates are different in each substrate. The binding events are almost over at t = 1000 s. The ΔR values at t = 1000 s in each MIM substrate are summarized in Table 6 along with calculated sensitivity, s, and evaluated avidin thickness, d_1 (nm). Variety d_1 values within acceptable range (0.8–1.9 nm) on MIM samples simply reflect slight differences in signal saturation. The binding events using the MIM substrates were probed with 2–4 times better sensitivity with respect to the AR measurements.

Table 6. ΔR for Binding of Avidin to Biotinylated Substrates in Water and Evaluated Thickness, d_1

d_2 (nm)	d_3 (nm)	ΔR (%)	s (% nm^{-1})	d_1 (nm)
0	0	1.0	0.6	1.6
10	80	−4.2	−2.2	1.9
15	40	2.2	1.8	1.2
15	55	3.2	3.0	1.1
15	80	3.5	4.5	0.8

Conclusion

We have shown here the theoretical and experimental results of biosensing using the MIM platform. The biosensing can be performed by a simple reflectivity measurement at normal incidence illumination without using bulky optical setup. According to the theoretical calculation, we conclude that MIM (10, 50) is the most suitable for the sensing in air and that MIM (10, 70) is the best in water. It should be noted that optimized condition for measurements in air and in water were different as suggested in theoretical calculation because of the difference in the ambient medium refractive indexes. The mass resolution of the MIM-based biosensing is an order of magnitude less than that of the ATR-based SPR biosensing. However, it has much better spatial resolution because light does not propagate along the surface in the MIM platform. This allows us to use this platform in high-density multichannel biochips. Further application using MIM-based biosensor such as multichannel protein detection and fabrication of biosensor using other combination of noble metals is now underway.

Supporting Information Available: Calculated R_0 and R/R_0 profiles in air and water. This material is available free of charge via the Internet at http://pubs.acs.org.

(29) Arai, T.; Kumar, P. K. R.; Rockstuhl, C.; Awazu, K.; Tominaga, J. *J. Opt. A: Pure Appl. Opt.* **2007**, *9*, 699–703.
(30) Vos, K. D.; Bartolozzi, I.; Schacht, E.; Bienstman, P.; Baets, R. *Opt. Express* **2007**, *15*, 7610–7615.
(31) Tang, Y.; Mernaugh, R.; Zeng, X. *Anal. Chem.* **2006**, *78*, 1841–1848.
(32) Nath, N.; Chilkoti, A. *Anal. Chem.* **2002**, *74*, 504–509.
(33) Nath, N.; Chilkoti, A. *J. Fluoresc.* **2004**, *14*, 377–389.

Optical Response of Gold-Nanoparticle-Amplified Surface Plasmon Resonance Spectroscopy

Yuichi Uchiho,[†] Masayuki Shimojo,[‡,§] Kazuo Furuya,[§] and Kotaro Kajikawa*[,†]

Interdisciplinary Graduate School of Science and Engineering, Tokyo Institute of Technology, Nagatsuta, Midori-ku, Yokohama 226-8502, Japan, Advanced Science Research Laboratory, Saitama Institute of Technology, 1690 Fusaiji, Fukaya, 369-0293, Japan, and High Voltage Electron Microscopy Station, National Institute for Materials Science, 3-13 Sakura, Tsukuba, 305-0003, Japan

Received: November 1, 2009; Revised Manuscript Received: January 19, 2010

A simple formalism that predicts optical constants of a two-dimensionally distributed nanoparticle (NP) thin film is presented for analysis of the NP-amplified surface plasmon resonance. The dielectric constant of the NP thin film can be evaluated with simple expressions at low coverages ($\sigma < 0.08$), whereas the local fields induced by surrounding polarizations of NPs should be taken into account at coverages of $\sigma > 0.08$. Analytical and numerical calculations are carried out for evaluating the local fields at different conditions. The Clausius−Mossoti relation, which is usually used for evaluation of dielectric constants of a binary medium, does not hold in the NP thin films, because of the large interparticle distance and/or the retardation effect. We carried out SPR measurements for NP films with different NP coverages, and the results support the proposed analytical formalism. Finally we propose a procedure to evaluate the NP coverage from the NP-SPR profile experimentally obtained.

I. Introduction

Two-dimensionally distributed metallic nanoparticle (NP) films immobilized on a surface have been extensively studied as a promising material for localized surface plasmons (LSPs).[1−19] For instance, NP-amplified surface plasmon resonance (NP-SPR) delivers a great improvement on the protein detection limit of SPR biosensors using an attenuated total reflection(ATR) geometry.[20−29] In this technique, immobilization of NPs at proteins binding to ligand produces a great change in the resonance angle of incidence at the surface plasmon condition. We have also reported considerably enhanced second-harmonic generation (SHG) in two-dimensionally distributed gold NPs[7,8] and its application to biosensors.[9] The enhancement of SHG is due to the generation of intensified electric fields at the resonance condition of LSPs in metallic NPs.

Optical properties of the two-dimensionally distributed metallic nanoisland films formed on a substrate have been investigated since 1970s.[31−35] The nanoisland films were fabricated through thermal annealing of ultrathin metallic films vacuum-evaporated on a dielectric substrate. The nanoislands are approximated to be rotational ellipsoids, the optical properties of which were predicted taking into account the interaction from dipole array of surrounding nanoislands formed in the substrate, under the local field approximation (LFA). However their calculation is not straightforward for the analysis of practical applications such as the LSP biosensing. Well-defined chemically synthesized spherical NPs are recently commercially available for LSP, and they are easily immobilized on a substrate by surfactant or biological molecules. Thereby a simple formalism that predicts the optical properties of the NP films is necessary.

In this paper we present a theoretical expression for NP-SPR spectroscopy. We consider a film consisting of spherical NPs located above a metallic surface with a nanogap, as shown in Figure 1a. Although there are several approximation methods for evaluating a optical constant of a layer consisted of two different materials, such as the effective medium approximation, they cannot predict the NP-SPR profiles sufficiently (See Figure 1S in the Supporting Information). When the NPs are very close to a metallic surface, the electromagnetic interaction between the NP and the metallic surface is significant.[5−8,19,36−38] We calculated the NP-SPR profiles taking into account the interparticle interaction and the multipole interaction between the NP and the substrate. In order to verify the adequacy of our theoretical expressions, we performed experimental NP-SPR measurements to evaluate the optical parameters of the NP films. We obtained agreement between the experimental and the theoretical, and conclude that our theoretical expressions can be used to explain the optical response in the NP-SPR measurements.

II. Theory

A. Polarizability of NP. We consider a NP system consisting of an ambient medium (relative dielectric constant ε_1), a substrate (relative dielectric constant ε_2), and a spherical gold NP (radius R and relative dielectric constant ε_3), as illustrated in Figure 1a. The dielectric constants ε_2 and ε_3 are generally frequency dependent, whereas the dispersion of ε_1 is negligible. The gap is supported by a thin dielectric layer with a dielectric constant ε_4. While isolated spherical NPs are optically isotropic, they are usually uniaxial with the optic axis in the surface normal direction, z. The anisotropy originates from the electromagnetic interactions between the NP and the metallic substrate. Light is incident on the surface with the $x-z$ plane of incidence. Polarizability of a NP, α_q is generally described as

$$\alpha_q = 4\pi\varepsilon_1 R^3 A_q \qquad (q = // \text{ or } z) \tag{1}$$

where // denotes the in-plane components, namely x or y. There are a number of methods to evaluate the parameter A_q. They

* To whom correspondence should be addressed. E-mail: kajikawa@ep.titech.ac.jp.
† Tokyo Institute of Technology.
‡ Saitama Institute of Technology.
§ National Institute for Materials Science.

10.1021/jp910438q
Published on Web 03/01/2010

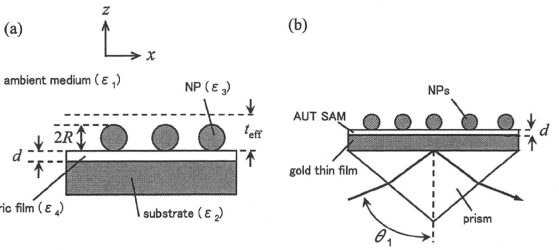

Figure 1. (a) Schematic illustration of the NP thin film. (b) The optical geometry for SPR experiments.

differ in degree of approximation. When spherical NPs can be regarded as of isolation, the polarizability is isotropic and the subscript q is suppressed. The parameter A is described as

$$A = -\frac{\varepsilon_1 - \varepsilon_3}{2\varepsilon_1 + \varepsilon_3} \tag{2}$$

In this expression, the contribution from the substrate and the supporting layer are ignored. Hence it is applied only to the limiting case that NPs are apart from the surface.

For calculating more accurate parameters of A, we need to consider the multipoles. This problem on the condition of $\varepsilon_4 = \varepsilon_1$ was solved by Wind et al.[38] We have slightly developed their formalism to take into account the contribution from the gap-supporting layer.[39] The jth order multipolar coefficients A_{qj} are calculated by the following equations:[2,38]

$$\sum_{j=1}^{\infty}\left\{\delta_{kj} + \frac{k(\varepsilon_2 - \varepsilon_1)(\varepsilon_1 - \varepsilon_3)}{[k\varepsilon_3 + (k+1)\varepsilon_1](\varepsilon_1 + \varepsilon_2)}\frac{(k+j)!}{k!j!(2r_z)^{k+j+1}}\right\}A_{zj} = \left(\frac{\varepsilon_1 - \varepsilon_3}{\varepsilon_1 + 2\varepsilon_3}\right)\delta_{k1} \qquad (k = 1, 2, 3, \ldots) \tag{3}$$

$$\sum_{j=1}^{\infty}\left\{\delta_{kj} + \frac{k(\varepsilon_2 - \varepsilon_1)(\varepsilon_1 - \varepsilon_3)}{[k\varepsilon_3 + (k+1)\varepsilon_1](\varepsilon_1 + \varepsilon_2)}\frac{(k+j)!}{(k+1)!(j-1)!(2r_{//})^{k+j+1}}\right\}A_{//j} = \left(\frac{\varepsilon_1 - \varepsilon_3}{\varepsilon_1 + 2\varepsilon_3}\right)\delta_{k1} \qquad (k = 1, 2, 3, \ldots) \tag{4}$$

where δ_{kj} is Kronecker's delta. Here, $r_z = 1 + (d\varepsilon_1)/(R\varepsilon_4)$ and $r_{//} = 1 + d/R$. The contribution of the gap layer is considered by using the thickness of the gap layer d divided by $\varepsilon_4/\varepsilon_1$ for the surface normal components of the electric fields. This is because the existence of the gap layer reduces the effective gap distance by a factor of $\varepsilon_4/\varepsilon_1$. The first order coefficient A_{q1} is responsible for the polarizability of NPs, i.e., $A_q = -A_{q1}$.

Figure 2 plots the real and imaginary parts of A_z and $A_{//}$ of the gold NPs on a gold surface in air, as a function of wavelength λ for different R/d values, using eqs 3 and 4. (See Figure 2S in Supporting Information for A_z and $A_{//}$ in water.) The multipoles until the 31st order were considered. The calculation was made with dielectric constants in literature.[40] The parameter A calculated by eq 2 corresponds to the profile at $R/d = 0$ because eq 2 is equivalent to the case of the infinity gap distance. At $R/d > 5$, another red-shifted band are observed as a sharp peak in the imaginary A_z profiles. The amount of redshift increases with R/d. Although the profiles in water are similar to that in air, the amount of redshift in the imaginary A_z profiles in water is larger than that in air. Most $A_{//}$ spectra in air have a single peak at around 510 nm. In contrast to the A_z profiles, the red-shifted peak is observed only in the profiles at $R/d \geq 10$ in water and at $R/d = 40$ in air as a shoulder.

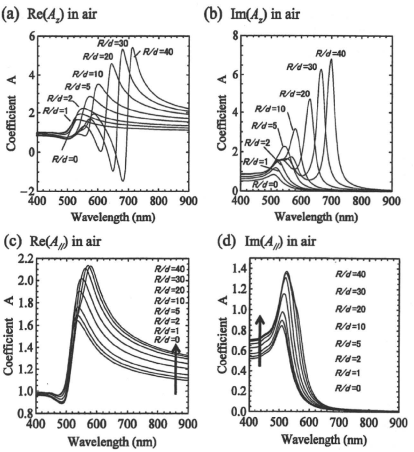

Figure 2. The parameter A_z and $A_{//}$ calculated using eqs 3 and 4 in air at different R/d ratios. (a) Real part of A_z. (b) Imaginary part of A_z. (c) Real part of $A_{//}$. (d) Imaginary part of $A_{//}$.

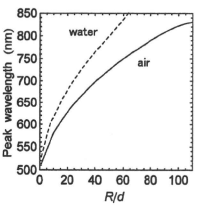

Figure 3. Peak wavelengths of the red-shifted band as a function of R/d for ambient of air and water.

Figure 3 shows the peak wavelengths of the red-shifted band in the A_z curve, with respect to R/d in air or in water. The NPs supported by a dielectric thin film ($\varepsilon_4 = 2.25$) are considered. Similar relation was shown in previous papers, where the contribu-

tion of the gap layer was ignored[30] or was taken into account using the effective ambient dielectric constant of 2.0 instead of 1.0.[5,7,8] However, they can predict only resonance wavelengths with these parameters and cannot evaluate the polarizability.

B. Dielectric Constant of NP Film. Here we regard the metallic NPs dispersed on a substrate as a thin film having an effective thickness t_{eff}. The effective thickness t_{eff} is arbitrary within the range much less than the wavelength of light. We assume that the NPs are point dipoles in regard to the interparticle electromagnetic interaction and the interparticle multipolar interaction is ignored. This is because the interparticle distance is usually large enough and the coverages of NPs in our experiments are low enough to satisfy this approximation. A detailed discussion of the interparticle interaction can be found in section II.C. The contribution of the mirror images formed in the substrate is taken in the parameter A. As a result, we can simply describe the optical properties of the spherical NP films as described below.

The polarization of a NP, $\mathbf{p}$, induced by a local electric field, $\mathbf{E}_{\text{loc}}$, is written as

$$\mathbf{p} = \varepsilon_0 \vec{\vec{\alpha}} \mathbf{E}_{\text{loc}} \tag{5}$$

where $\vec{\vec{\alpha}}$ is a polarizability tensor of the NP and ε_0 is the vacuum permittivity. The tensor $\vec{\vec{\alpha}}$ is diagonal and has two independent components $\alpha_{//} = \alpha_{xx} = \alpha_{yy}$ and $\alpha_z = \alpha_{zz}$, since NPs are generally uniaxial with the optic axis in the surface normal direction. The local field $\mathbf{E}_{\text{loc}}$ at the original point generally differs from the external electric field $\mathbf{E}_{\text{ext}}$ of the incident light and is described as[41-43]

$$\mathbf{E}_{\text{loc}} = \mathbf{E}_{\text{ext}} + \frac{1}{4\pi\varepsilon_0\varepsilon_1} \sum_i \left(\frac{3\mathbf{n}_i\mathbf{n}_i - 1}{r_i^3} \right) \mathbf{p}_i \tag{6}$$

Here $\mathbf{n}_i$ is the unit vector pointing from a surrounding dipole i (dipole moment $\mathbf{p}_i$) to the original point and r_i is the distance between the dipole and the original point. Since each dipole is considered to be equivalent, we can use the LFA. Then the local field $\mathbf{E}_{\text{loc}}$ can be written as

$$\mathbf{E}_{\text{loc}} = \mathbf{E}_{\text{ext}} + \frac{1}{4\pi\varepsilon_0\varepsilon_1} \vec{\vec{\Xi}} \mathbf{p} \tag{7}$$

The tensor $\vec{\vec{\Xi}}$ is an operator to sum up the electric fields induced by the surrounding dipoles. A local field factor tensor $\vec{\mathbf{L}}$ is introduced to connect them as $\mathbf{E}_{\text{loc}} = \vec{\mathbf{L}}\mathbf{E}_{\text{ext}}$. The $\vec{\mathbf{L}}$ tensor is diagonal and generally has three independent components L_{xx}, L_{yy}, and L_{zz}, and using eqs 5 and 7, $\vec{\mathbf{L}}$ is written as

$$\vec{\mathbf{L}} = \left(\vec{\mathbf{I}} - \frac{1}{4\pi\varepsilon_1} \vec{\vec{\Xi}} \vec{\vec{\alpha}} \right)^{-1} \tag{8}$$

where $\vec{\mathbf{I}}$ is the unit tensor. The tensor $\vec{\vec{\Xi}}$ is diagonal and generally has three independent components Ξ_{xx}, Ξ_{yy} and Ξ_{zz}. Details of the tensor $\vec{\vec{\Xi}}$ is discussed in the next section.

The macroscopic polarization $\mathbf{P}$ can be expressed as

$$\mathbf{P} = N\mathbf{p} \tag{9}$$

where N is a volume number density of polarization. The surface number density, N_s, is more essential than N for two-dimensional systems. Hence we will use N_s, instead of N, using the relation $N_s = t_{\text{eff}}N$.

The flux density of NPs layer, $\mathbf{D}$, can be expressed as

$$\mathbf{D} = \varepsilon_0\boldsymbol{\varepsilon}\mathbf{E} = \varepsilon_0\varepsilon_1\mathbf{E} + \mathbf{P} \tag{10}$$

where $\mathbf{E}$ represents the electric field of the NP layer and $\boldsymbol{\varepsilon}$ represents the dielectric tensor of the NP layer. We added ε_1 in eq 10 because without any NPs ($\mathbf{P} = 0$), the dielectric constant, $\boldsymbol{\varepsilon}$, should be same as that of an ambient medium, ε_1. Then eq 10 can be transformed as following expression using eqs 5, 7, and 9.

$$\begin{aligned} \varepsilon_0\boldsymbol{\varepsilon}\mathbf{E} &= \varepsilon_0\varepsilon_1\mathbf{E} + N\varepsilon_0\vec{\vec{\alpha}}\mathbf{E}_{\text{loc}} \\ &= \varepsilon_0\varepsilon_1\mathbf{E} + N\varepsilon_0\vec{\vec{\alpha}}\vec{\mathbf{L}}\mathbf{E}_{\text{ext}} \end{aligned} \tag{11}$$

Since the surface normal component of electric flux density is continuous at the boundary ($\varepsilon_z E_z = \varepsilon_1 E_{\text{ext},z}$), we have the surface normal component of the relative dielectric constant of the NP film, ε_z, as

$$\varepsilon_z = \varepsilon_1 \left(1 - \frac{1}{\varepsilon_1} N\alpha_z L_{zz} \right)^{-1} = \varepsilon_1 \left(1 - \frac{1}{\varepsilon_1} \left(\frac{N_s}{t_{\text{eff}}} \right) \alpha_z L_{zz} \right)^{-1} \tag{12}$$

The continuity of the in-plain electric field ($E_{//} = E_{\text{ext},//}$) yields the in-plain component, $\varepsilon_{//}$,

$$\varepsilon_{//} = \varepsilon_1 + N\alpha_{//}L_{//} = \varepsilon_1 + \left(\frac{N_s}{t_{\text{eff}}} \right) \alpha_{//}L_{//} \tag{13}$$

Although t_{eff} is arbitrary, one of the most reasonable and convenient choice is $t_{\text{eff}} = 2R$. Then we can directly relate the dielectric constant of the thin film to the coverage of the NPs, σ, using the relation $\sigma = N_s\pi R^2$ and eq 1. Then, eq 12 is rewritten as

$$\varepsilon_z = \varepsilon_1 \left(1 + \frac{2\sigma A_z L_{zz}}{1 - 2\sigma A_z L_{zz}} \right) \tag{14}$$

and similarly eq 13 is

$$\varepsilon_{//} = \varepsilon_1 (1 + 2\sigma A_{//} L_{//}) \tag{15}$$

C. $\vec{\vec{\Xi}}$ Components. First we consider the tensor $\vec{\vec{\Xi}}$ in the absence of retardation. When NPs are too close (the gap between the NPs is less than the diameter of the particles: $a < 4R$ in square lattice), the interparticle multipolar interaction cannot be neglected and the local field cannot be written by the simple dipolar form written by eq 6. This is the case that $\sigma > \pi R^2/(4R)^2 \sim 0.2$. Thus we will treat the case that the interparticle multipolar interaction can be neglected ($\sigma < 0.2$), hereafter.

For a two-dimensional square lattice with a lattice constant a ($a > 4R$), the tensor $\vec{\vec{\Xi}}^{\text{sq}}$ is composed of two independent diagonal components[41-43]

$$\Xi_z^{\text{sq}} = \Xi_{zz}^{\text{sq}} = \frac{\xi_z^{\text{sq}}}{a^3} = (N_s^{\text{sq}})^{3/2} \xi_z^{\text{sq}} \tag{16}$$

and

$$\Xi_{//}^{sq} = \Xi_{xx}^{sq} = \Xi_{yy}^{sq} = \frac{\xi_{//}^{sq}}{a^3} = (N_s^{sq})^{3/2}\xi_{//}^{sq} \qquad (17)$$

where the relation $N_s^{sq} = a^{-2}$ was used. The ξ values for a square lattice are given in literature:[44] $\xi_z^{sq} = -9.034$ and $\xi_{//}^{sq} = -\xi_z^{sq}/2$. The parameters for a hexagonal lattice with a lattice constant a are also given: $\xi_z^{hex} = -11.034$ and $\xi_{//}^{hex} = -\xi_z^{hex}/2$. The relation $N_s^{hex} = (2/\sqrt{3})(1/a^2)$ allows us to give the component Ξ_q^{hex}

$$\Xi_q^{hex} = \frac{\xi_q^{hex}}{a^3} = \left(\frac{\sqrt{3}}{2}N_s^{hex}\right)^{3/2}\xi_q^{hex} \cong (N_s^{hex})^{3/2}\xi_q^{sq}$$
$$(q = // \text{ or } z) \qquad (18)$$

Equation 18 implies that the Ξ components solely depend on N_s and ξ_q^{sq}. To verify this, we evaluated Ξ components in a two-dimensional system consisting of randomly distributed NPs. The procedure of the calculation is as follows: (1) A square with a dimension of 202 × 202 is considered. A NP of unity diameter is put at the center of the square, which is defined as the original point. (2) NPs of unity diameter are randomly placed on the square to make the interparticle distances be more than twice the diameter of the NP, in order to neglect the interparticle multipolar interaction. (3) The NP at the original point is removed, and the electric fields at the original point induced by the surrounding dipoles are summed up to have the tensor Ξ. In this calculation, 2×10^5 positions are randomly generated, and 6278 ± 14.8 NPs are placed without overlapping. This corresponds to $N_s^{ran} = 0.1539 \pm 0.000363$ and the corresponding coverage $\sigma = 0.1233 \pm 0.00029$. Iteration of 10 times yields the mean values of Ξ: $\Xi_{//}^{ran} = 0.268 \pm 0.138$ and $\Xi_z^{ran} = -0.5634 \pm 0.0739$. The distribution of the in-plane component $\Xi_{//}^{ran}$ is almost twice as large as that of the normal component Ξ_z^{ran}. This is because the in-plane component is strongly affected by the position of adjacent surrounding dipoles. With these results, we have the relations

$$\Xi_z^{ran} = -0.5634 \cong (N_s^{ran})^{3/2}\xi_z^{sq} \qquad (19)$$

and

$$\Xi_{//}^{ran} = 0.268 \cong (N_s^{ran})^{3/2}\xi_{//}^{sq} \qquad (20)$$

These results allow us to conclude that Ξ solely depends on N_s, and that one may use a two-dimensional square lattice without losing generality for evaluation of the Ξ tensor components.

Next, we consider the retardation effect. We only consider the square lattice below since it can be used as a general case. We performed numerical calculations for square lattice having 4×10^5 (201 × 201) dipoles to evaluate ξ components. The incident light at wavelength λ is directed onto the surface, where the plane of incidence is $x-z$ plane. The electric fields at the original point induced by the surrounding dipoles are added and complex ξ values are calculated. Because of the retardation effect, the in-plane components ξ_x and ξ_y are different; there are generally three independent ξ components. The ξ values are plotted as a function of λ/a at 0° and 45° angles of incidence in Figure 4. At normal incidence ξ_x and ξ_y are degenerated. In the region $(\lambda/a) \geq 50$, the retardation effect is so small that we can use the static ξ values, $\xi_z^{sq} = -2\xi_{//}^{sq} = -9.034$. However this is only limited cases that small NPs ($R \lesssim 3$ nm) are distributed with coverages $\sigma \leq 0.2$. In region $(\lambda/a) \leq 50$, the ξ values are complex and considerably depend on the value (λ/a). Therefore the ξ values should be calculated in general. However as described in the next section, we can regard the local field factor to be unity at coverages $\sigma \leq 0.08$. Therefore the ξ values including the retardation effect is needed in the cases that $0.08 \leq \sigma \leq 0.2$.

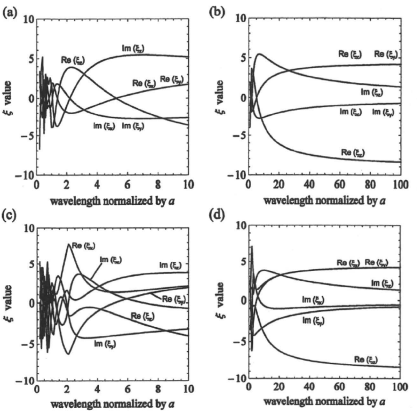

Figure 4. The parameter ξ including the retardation effect, as a function of normalized wavelength λ/a. (a) The ξ parameter at wavelengths $0 < \lambda/a < 10$ at normal incidence. (b) The ξ parameter at wavelengths $0 < \lambda/a < 100$ at normal incidence. (c) The ξ parameter at wavelengths $0 < \lambda/a < 10$ at 45° angle of incidence. (d) The ξ parameter at wavelengths $0 < \lambda/a < 100$ at 45° angle of incidence.

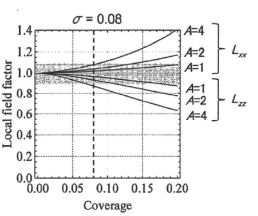

Figure 5. Local field factor as a function of coverage at different A values.

D. NP Film at Low Coverage. Using the relation, $\sigma = N_s\pi R^2$, and eq 8, L_{ii} is written as

$$L_{ii} = \left(1 - \left(\frac{\sigma}{\pi}\right)^{3/2}\xi_i^{sq}A_i\right)^{-1} \qquad (i = x, y \text{ or } z) \qquad (21)$$

Figure 5 shows the local field factors calculated as a function of σ at various A values, using eq 21. Since the parameter A is usually less than 2 under off-resonance conditions and the static ξ^{sq} values are the maximum, one may use the local field factor $L_q \sim 1$ for $\sigma < 0.08$ within deviation of 10%. At this low

coverage, eqs 14 and 15 can be written in the following simple forms

$$\varepsilon_z = \varepsilon_1\left(1 + \frac{2\sigma A_z}{1 - 2\sigma A_z}\right) \tag{22}$$

and

$$\varepsilon_{//} = \varepsilon_1(1 + 2\sigma A_{//}) \tag{23}$$

The dielectric constants of a NP film are described as a function of the parameters A and σ.

E. Comparison with the Clausius−Mossoti Relation. Substituting eq 21 into eq 12, the dielectric constant ε_z is written

$$\varepsilon_z = \frac{\varepsilon_1\left(1 - \frac{N_s^{3/2}\xi_z\alpha_z}{4\pi\varepsilon_1}\right)}{1 - \frac{N_s^{3/2}\xi_z\alpha_z}{4\pi\varepsilon_1} - \frac{N_s}{t_{\text{eff}}}\frac{\alpha_z}{\varepsilon_1}} = \frac{\varepsilon_1\left(1 - \left(\frac{\sigma}{\pi}\right)^{3/2}\xi_z A_z\right)}{1 - \left(\frac{\sigma}{\pi}\right)^{3/2}\xi_z A_z - 2\sigma A_z} \tag{24}$$

Similary, substituting eq 21 into eq 13, the dielectric constant $\varepsilon_{//}$ is written

$$\varepsilon_{//} = \frac{\varepsilon_1 - \frac{N_s^{3/2}\xi_{//}\alpha_{//}}{4\pi} + \frac{N_s}{t_{\text{eff}}}\alpha_{//}}{1 - \frac{N_s^{3/2}\xi_{//}\alpha_{//}}{4\pi\varepsilon_1}}$$

$$= \frac{\varepsilon_1\left(1 - \left(\frac{\sigma}{\pi}\right)^{3/2}\xi_{//}A_{//} + 2\sigma A_{//}\right)}{1 - \left(\frac{\sigma}{\pi}\right)^{3/2}\xi_{//}A_{//} - 2\sigma A_{//}} \tag{25}$$

Ui et al. reported that the relations are approximated to the Clausius−Mossoti relation if one sets $t_{\text{eff}} = a$ in the absence of the retardation effect.[43] With $t_{\text{eff}} = a$, eqs 24 and 25 are reduced to

$$\varepsilon_z = \varepsilon_1\frac{1 - \left(\frac{\xi_z}{4\pi}\right)\frac{N\alpha_z}{\varepsilon_1}}{1 - \left(\frac{\xi_z}{4\pi} + 1\right)\frac{N\alpha_z}{\varepsilon_1}} \sim \varepsilon_1\frac{1 + \frac{2}{3}\frac{N\alpha_z}{\varepsilon_1}}{1 - \frac{1}{3}\frac{N\alpha_z}{\varepsilon_1}} \tag{26}$$

and

$$\varepsilon_{//} = \varepsilon_1\frac{1 + \left(1 - \frac{\xi_{//}}{4\pi}\right)\frac{N\alpha_{//}}{\varepsilon_1}}{1 - \left(\frac{\xi_{//}}{4\pi}\right)\frac{N\alpha_{//}}{\varepsilon_1}} \sim \varepsilon_1\frac{1 + \frac{2}{3}\frac{N\alpha_{//}}{\varepsilon_1}}{1 - \frac{1}{3}\frac{N\alpha_{//}}{\varepsilon_1}} \tag{27}$$

Then the two-dimensional polarization sheet can be regarded as a slice of bulk with a thickness of a, having the same dielectric constant as that of bulk. This argument is useful for monomolecular layers, but is not applicable to NP films, because of the large interparticle distance (<100 nm) and the retardation effect. Accordingly, application of the Clausius-Mossoti relation to NP systems is usually irrelevant.

F. Effective Dielectric Constant of NP Film with Anisotropy. Since the procedure described above predicts the dielectric constant of the NP film, we can calculate the optical response using the transfer matrix method which is usually used for multilayer systems. The NP film is generally uniaxial with the optic axis in the surface normal direction. Hence we can use the transfer matrix method for isotropic medium by using the effective dielectric constant of the uniaxial NP layer ε_{NP}

$$\varepsilon_{\text{NP}} = \frac{\varepsilon_z\varepsilon_{//} + \varepsilon_1 \sin^2\theta_1(\varepsilon_z - \varepsilon_{//})}{\varepsilon_z} \tag{28}$$

where ε_{NP} varies with the angle of incidence, θ_1. For fitting of the experimental SPR curve to the theoretical one, ε_{NP} can be written by the parameters A and σ.

$$\begin{aligned}\varepsilon_{\text{NP}} &= \varepsilon_1(1 + 2\sigma A_{//} + \sin^2\theta_1(2\sigma(A_z - A_{//}) + 4\sigma^2 A_z A_{//})) \\ &\cong \varepsilon_1(1 + 2\sigma(A_{//}\cos^2\theta_1 + A_z \sin^2\theta_1))\end{aligned} \tag{29}$$

The approximation $4\sigma^2 A_z A_{//} = 0$ is valid for small σ. Then the SPR curve can be fitted with the single parameter of σ, since A_z, $A_{//}$ and $t_{\text{eff}} = 2R$ are known.

III. Calculation

On the basis of the analytical expressions described above, we computed the SPR profiles using the transfer matrix method.[45] First we calculated reflectivity of NP (5 nm in diameter) films supported by a gap-supporting layer 5 nm thick ($\varepsilon_4 = 2.25$), which is the typical dimension of proteins. The gap-supporting layer is placed on a 50 nm-thick gold film deposited at the bottom of a rectangular glass prism (refractive index 1.5). For evaluation of the dielectric constant of the NP film, the parameters of A were calculated using eq 2, which are plotted in Figure 2. This is good approximation to the case that the NP diameter is less than 10 nm, since the A profiles of eq 2 are similar to those of eq 3 and eq 4 at $R/d \leq 1.0$, within an error of less than 5%. We consider an incomplete gap-supporting layer (submonolayer) with the effective dielectric constant, $\varepsilon_{4,\text{eff}}$, at coverage σ, which is estimated by the following expression:

$$\varepsilon_{4,\text{eff}} = \sigma\varepsilon_4 + (1 - \sigma)\varepsilon_1 \tag{30}$$

where ε_4 (= 2.25) is the relative dielectric constant of the complete gap-supporting layer (see Figure 3S in the Supporting Information about comparison between eq 30 and effective medium approximation, and little difference exists between the dielectric constants by the two methods). For simplicity, the coverage of the gap-supporting material and the NPs was assumed to be identical. Figure 6 plots the SPR profiles at different NP coverages and at wavelength 635 nm in air (See Figure 4S in the Supporting Information for different wavelength 835 nm and water). The resonance angle increases with σ, and the minimum reflectivity almost stays zero at any σ values. This SPR shift is due to the increase in the real part of ε_{NP}. The amount of the SPR shift in water is slightly larger than those in air. In the profiles of 835 nm, the amount of the SPR shifts is

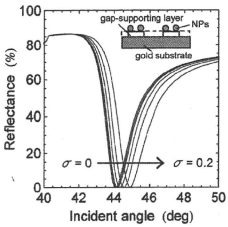

Figure 6. Calculated SPR profiles at different coverages $\sigma = 0$, 0.01, 0.02, 0.05, 0.1, and 0.2 at $\lambda = 635$ nm in air.

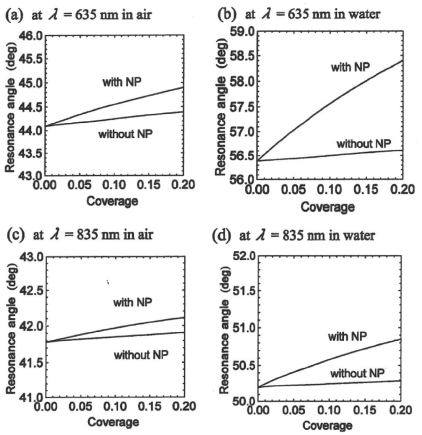

Figure 7. Resonance angles as a function of coverage, at $\lambda = 635$ nm in air (a), $\lambda = 635$ nm in water (b), $\lambda = 835$ nm in air (c), and $\lambda = 835$ nm in water (d).

smaller than that of the corresponding shifts at 635 nm. In either case, the obvious broadening in the SPR dip is not observed which has been often reported. This is because the electromagnetic interaction between the NP and the substrate, which is the origin of the broadening, is not taking into account in this calculation.

The resonance angles, θ_r, are plotted as a function of the NP coverage in Figure 7. The resonance angles in the absence of NPs are also plotted, in which the effective dielectric constant of the gap-supporting layer is calculated using eq 30. The NP-SPR at 635 nm in air shows a shift of 0.81 degree at $\sigma = 0.2$, whereas the shift due to presence of 5 nm dielectric film at the same coverage is only 0.30 degrees in the absence of NPs. This means that the sensitivity is enhanced by a factor of 2.7 on adsorption of NPs. The mean change rates of the resonance angle with respect to the coverage, $\Delta\theta_r/\Delta\sigma$, are listed in Table 1 at various conditions. The rate is defined as

$$\frac{\Delta\theta_r}{\Delta\sigma} = \frac{\theta_r(\sigma_1) - \theta_r(0)}{\sigma_1} \tag{31}$$

We calculated with $\sigma_1 = 0.2$; unless the SPR dip disappears at high coverage for heavy broadening, where the highest σ_1

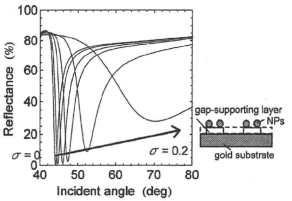

Figure 8. Calculated SPR profiles at different coverages = 0, 0.01, 0.03, 0.05, 0.1, and 0.2 at = 635 nm in air. The thickness of the gap-supporting layer $d = 5$ nm and $R = 25$ nm.

TABLE 1: Mean Change in the Resonance Angle of the Films with or without NPs[a]

wavelength (nm)	ambient	NPs	$\Delta\theta_r/\Delta\sigma$ deg
635	air	w/o	1.5
635	air	w	4.05
635	water	w/o	1.1
635	water	w	10.05
835	air	w/o	0.65
835	air	w	1.65
835	water	w/o	0.45
835	water	w	3.25

[a] The NPs are assumed to be isolated and eq 2 was used for calculation of A. "w" and "w/o" in the NPs column mean "with NPs" and "without NPs", respectively.

that gives a SPR dip was used. The enhancement factors are about 2−3 in air and 7−10 in water. This is in agreement with the results in the previous study, in which NPs ($R = 5$ nm) were used to intensify the signal from IgG.[21]

Next we computed the SPR profiles, taking into account the contribution of the substrate. Figure 8 shows the SPR profiles of the NP films at $R = 25$ nm, and $\lambda = 635$ nm (see Figure 5S for different sizes of NPs). The gap-supporting layer 5 nm thick is considered. The local field factor L_g is unity in the case of $\sigma \leq 0.08$, as described in Section II D. In the case of $0.08 \leq \sigma \leq 0.2$, we calculated the ξ components for the incident angles with taking into account the retardation effect as described in section II.C. Both broadening and an increase in the minimum reflectivity are observed in the profiles at $R = 25$, 40, and 75 nm at high coverages. This is due to a large imaginary part of the dielectric constant of the NP film. The calculated resonance angle, θ_r, is plotted as a function of the coverage at $R = 5$, 15, 25, 40, and 75 nm in Figure 9. It should be noted that, although long-wavelength approximation (retardation effect) is not held for $R = 75$ nm, we show the results of $R = 75$ nm since they are qualitatively adequate. The θ_r profiles at 635 nm in air and in water are shown in Figure 9, panels a and b, respectively, and the profiles at 835 nm in air and in water are shown in Figure 9, panels c and d. At a given coverage, large NPs give a great change in θ_r. This is due to the large effective thickness, $2R$ and the large real part of A. However, the broader SPR dip with negative shift in water at $R = 75$ nm and $\lambda = 635$ nm are observed, as increasing the coverage (Figure 10a). This strange behavior is caused by the small negative real part of A_z at $\lambda = 635$ nm and $R/d = 15$ as shown in the spectrum of parameter A_z (Figure 10b). The mean rates of $\Delta\theta_r/\Delta\sigma$ are listed in Table 2 at different R values. Mostly the rate increases with NP size. The largest rate 433 is given at $R = 75$ nm and $\lambda = 635$ nm. The electromagnetic interaction between the NPs and the substrate produces the great enhancement in NP-SPR.

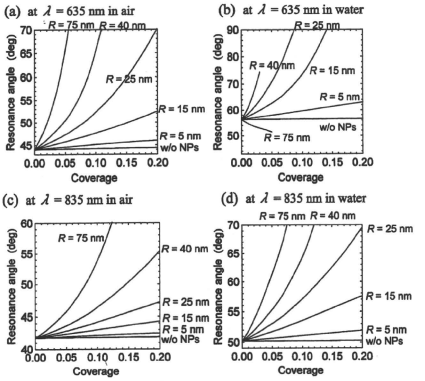

Figure 9. Resonance angle as a function of coverage for different R. (a) $\lambda = 635$ nm in air, (b) $\lambda = 635$ nm in water, (c) $\lambda = 835$ nm in air, and (d) $\lambda = 835$ nm in water.

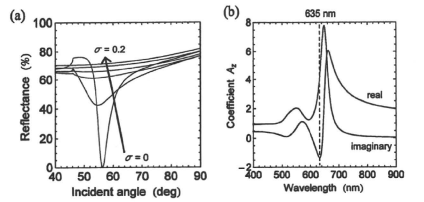

Figure 10. (a) Calculated SPR profiles ($R = 75$ nm) at different coverages $\sigma = 0$, 0.01, 0.03, 0.05, 0.1, and 0.2 at $\lambda = 635$ nm in water. The thickness of the gap-supporting layer $d = 5$ nm. (b) The parameter A_z calculated at $R/d = 15$.

According to the calculated results, we found the conditions that give a large enhancement of the NP-SPR. Larger NP sizes give greater enhancement of the SPR signal unless the LSP is on resonance at the illumination light wavelength. If the LSP is on resonance, the peak shift upon adsorption or binding to the analyte is not great because of the small real part of the polarizability. To avoid this, we had better use an illumination wavelength in near-infrared region, for instance, using a semiconductor laser line at 835 nm.

IV. Experimental Section

The sample used in this study is illustrated in Figure 1b. Thin gold films were prepared on a silica slide used as a substrate by vacuum evaporation at a pressure of 10^{-4} Pa. A 1 nm-thick chromium thin film was deposited between the gold film and the silica slide to promote adhesion of the gold film to the substrate. The 11-amino-1-undecanethiol (AUT) self-assembled monolayer (SAM) purchased from Dojindo Laboratory, Japan was dissolved in ethanol at a concentration of 0.1 mM. Successively AUT SAMs were prepared by immersion of the gold substrate in the solution for 1 h, followed by rinsing with ethanol. The AUT-covered gold substrate was immersed in an aqueous solution of gold NPs 50 nm in diameter (Tanaka Kikinzoku K.K., Japan). The samples were prepared with immersion time of 30, 300, and 3000 s. The substrate was then rinsed with pure water. A field emission scanning electron microscope (FE-SEM) was used to evaluate the surface number density of the gold nanoparticles.

TABLE 2: Mean Change in the Resonance Angle of the NP Films[a]

wavelength (nm)	ambient	R (nm)	$\Delta\theta_r/\Delta\sigma$ deg
635	air	w/o	1.5
635	air	5	9.55
635	air	15	42.2
635	air	25	131.1
635	air	40	213.2
635	air	75	433
635	water	w/o	1.1
635	water	5	32.85
635	water	15	168.9
635	water	25	287.8
635	water	40	598
635	water	75	−98.8
835	air	w/o	0.65
835	air	5	3.5
835	air	15	12.45
835	air	25	27.05
835	air	40	68.35
835	air	75	120.3
835	water	w/o	0.45
835	water	5	8.6
835	water	15	36.75
835	water	25	96.65
835	water	40	141.2
835	water	75	221.6

[a] The NPs (radius R) are assumed to be located above a gold surface with a gap distance of 5 nm. Equations 3 and 4 were used for calculation of A. "w/o" in the R column means "in the absence of NPs".

The SPR spectroscopy was carried out in the attenuated total reflection (ATR) geometry. A rectangular BK7 prism was used for the coupling of surface plasmons. Two kinds of semiconductor lasers (635 and 835 nm) were used. A couple of polarizers were used to choose the illumination polarization and to control the illumination intensity. The reflected light was detected with a silicon photodiode, and the signal was recorded with a 12-bit A/D converter board installed in a computer that controlled the sample stages.

V. Results and Discussion

In order to test the theory described above, we performed SPR measurements for the samples having different NP coverages. Figure 11 shows the SEM images of the samples prepared for different immersion times 30 s, 300 and 3000 s. They are respectively denoted as sample I, II and III. The coverages of NPs were evaluated from the SEM images and are summarized in Table 3. The images show that the interparticle distances are enough to neglect the interparticle interactions, which is not significant when $\sigma < 0.2$. Hence the small coverage in each sample allows us to use the simple formalism given in eq 22 and eq 23.

The NP-SPR curves were captured at 635 nm for samples I–III. Figure 12a shows the SPR curve for an AUT-covered thin gold film in the absence of NPs, for reference. The experimental curves for samples I–III are shown with solid lines in Figure 12b–d (see also Figure 1S in the Supporting Information for the calculation results by effective medium approximation). To calculate the parameter A_q for samples I–III, the gap distance d was estimated with the p-polarized transmission absorption spectra at 60° incidence. From the absorption

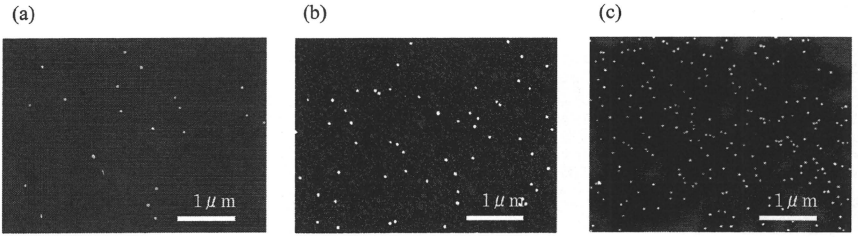

Figure 11. SEM images for immersion time (a) 30, (b) 300, and (c) 3000 s.

TABLE 3: Coverages Evaluated by SEM Microscopy and Dielectric Constants of the NP Films for Each Sample

sample	coverage σ	ε_z	$\varepsilon_{//}$
I	0.0023	$1.00143 + 0.00367i$	$1.00401 + 0.00022i$
II	0.0075	$1.00451 + 0.00120i$	$1.01290 + 0.00071i$
III	0.032	$1.01650 + 0.05390i$	$1.05460 + 0.00293i$

spectrum, the evaluated gap distance of the AUT SAM to be 0.75 nm and its standard deviation of 0.21 nm was used. The details to determine these parameters are described in a previous paper.[39] Then assuming the normal distribution of the gap distance, the SPR curves were calculated by the transfer matrix method, as shown with broken lines in Figure 12b–d. One may see the agreement on the resonance angles between the experiments and the calculations. This indicates that this theory is applicable to evaluate the dielectric constant of NP film. The resonance angle scarcely changes in spite of the increase in σ. This is because the real part of A_z is small at $R/d = 33$ and the real part of ε_z is almost unchanged with σ, as shown in the calculated A_z spectrum (Figure 13a). On the other hand, the imaginary part of ε_z increases with σ, resulting in the broadening of the SPR dip.

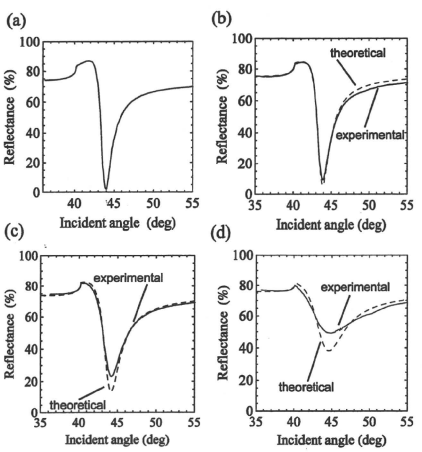

Figure 12. SPR profile measured (solid line) and calculated (broken line) for (a) AUT-covered Au, (b) sample I, (c) sample II, and (d) sample III.

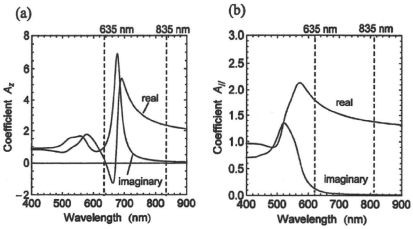

Figure 13. The parameter A calculated at $R/d = 33$. (a) In-plain component $A_{//}$ and (b) normal component A_z.

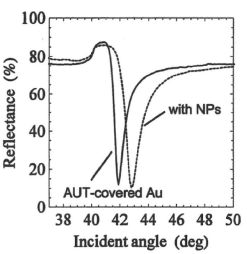

Figure 14. SPR profile measured for sample IV. (a) without any NP film (b) with the NP film.

In order to support the results shown above, we prepared another sample prepared in the same manner as we did for sample III (denoted as sample IV). Figure 14 shows the SPR profiles at 835 nm for sample IV and the gold thin film in the absence of NPs. On the contrary to the SPR profiles at 635 nm, the SPR dip is shifted to larger incident angle without broadening. This is due to the small imaginary part of the parameter A at 835 nm, as shown in Figure 13. Since the parameter A_q is obtained, we can obtain σ from the SPR curve. The coverage was evaluated to be 0.036 and this was almost same as that of sample III. The SPR profile at 835 nm shows a obvious shift of the resonance angle compared to that of 635 nm since the wavelength of 835 nm is on off-resonance (Figure 13b).

VI. Conclusion

A simple formalism that predicts optical constants of a two-dimensionally distributed NP thin film is presented. The dielectric constant can be evaluated with the simple expressions given in eqs 22 and 23, at low coverages ($\sigma < 0.08$). Otherwise,

the local field effect should be taken into account for evaluating the dielectric constant ($0.08 < \sigma < 0.2$). The ξ values including the retardation effect is given in Figure 4. Although the dipole sum-up operator Ξ depends on the lattice structure, we showed that Ξ for the square lattice can be used without losing generality. We also showed that the Clausius-Mossoti relation does not necessarily hold in the two-dimensionally distributed NP thin film. We performed SPR measurements for the NP films with different coverages and had agreements between the experimental and the calculated profiles. The results show that our formalism is useful for extracting the optical properties of two-dimensionally distributed metallic NP films on a surface and NP-SPR biosensing.

Using the formalism proposed, we found that large NPs mostly give better amplification factors in the NP-SPR biosensing upon adsorption of NPs at $\lambda = 835$ nm. However, if the parameter A_z is at near resonance, large NPs do not always give large amplification. Careful choice based on the formalism presented in this paper is necessary.

Finally we propose a recipe to evaluate the number of NPs in the NP-SPR biosensing. (i) When the gap distance is unknown, one should measure the red-shifted LSP peak wavelength by absorption spectroscopy.[39] The gap distance with respect to the peak wavelength is found in Figure 3. (ii) Evaluate the A_z and $A_{//}$ values using Figure 2, in which the A_q values are shown as a function of the wavelength or R/d. (iii) Estimate the appropriate value of σ. We can fit the theoretical SPR curve to the experimentally obtained one using the dielectric constant of the NP film, ε_{NP} given by eq 29, using the transfer matrix method. Since the parameter A is given by calculation, only a fitting parameter is σ.

Supporting Information Available: Figure 1S: Comparison of SPR profiles between measured and calculated by the effective medium approximation. Figure 2S: The parameter A_z and $A_{//}$ in water. Figure 3S: The dielectric constants calculated by a linear combination and EMA. Figure 4S: Calculated SPR profiles for different wavelength and different ambient medium. Figure 5S: Calculated SPR profiles taking into account the contribution of the substrate for different size of NPs. This material is available free of charge via the Internet at http://pubs.acs.org.

References and Notes

(1) Bohren, C. F.; Huffman, D. R. *Absorption and Scattering of Light by Small Particles*; Wiley: NewYork, 1983.
(2) Kawata, S., Ed.; *Near-Field Optics and Surface Plasmon Polaritons*: Springer: Berlin, 2001.
(3) Meriaudeau, F.; Downey, T. R.; Passian, A.; Wig, A.; Ferrell, T. L. *Appl. Opt.* **1998**, *37*, 8030.
(4) Okamoto, T.; Yamaguchi, I.; Kobayashi, T. *Opt. Lett.* **2000**, *25*, 372.
(5) Okamoto, T.; Yamaguchi, I. *J. Phys. Chem. B* **2003**, *107*, 10321.
(6) Kume, T.; Hayashi, S.; Yamamoto, K. *Phys. Rev. B* **1997**, *55*, 4774.
(7) Abe, S.: Kajikawa, K. *Phys. Rev. B* **2006**, *74*, 035416.
(8) Tsuboi, K.; Abe, S.: Fukuba, S.; Shimojo, M.; Tanaka, M.; Furuya, K.; Fujita, K.; Kajikawa, K. *J. Chem. Phys.* **2006**, *125*, 174703.
(9) Tsuboi, K.; Fukuba, S.; Naraoka, R.; Fujita, K.; Kajikawa, K. *Appl. Opt.* **2007**, *46*, 4486.
(10) Gupta, G.; Tanaka, D.; Ito, Y.; Shibata, D.; Shimojo, M.; Fukuya, K.; Mitsui, K.; Kajikawa, K. *Nanotechnology* **2009**, *20*, 25703.
(11) Mitsui, K.; Handa, Y.; Kajikawa, K. *Appl. Phys. Lett.* **2004**, *85*, 4231.
(12) Holland, W. R.; Hall, D. G. *Phys. Rev. Lett.* **1984**, *52*, 1041.
(13) Endo, T.; Yamamura, S.; Nagatani, N.; Morita, Y.; Takamura, Y.; Tamiya, E. *Sci. Tech. Adv. Mater.* **2005**, *6*, 491.
(14) Nath, N.; Chilkoti, A. *Anal. Chem.* **2002**, *74*, 504.
(15) Nath, N.; Chilkoti, A. *Anal. Chem.* **2004**, *76*, 5370–5378.
(16) Ghosh, S. K.; Pal, T. *Chem. Rev.* **2007**, *107*, 4797.
(17) Homola, J. *Chem. Rev.* **2008**, *108*, 462.
(18) Fan, X.; White, I. M.; Shopova, S. I.; Zhu, H.; Suter, J. D.; Sun, Y. *Anal. Chim. Acta* **2008**, *620*, 8.
(19) Xu, H.; Käll, M. *Sens. Actuators B* **2002**, *87*, 244.
(20) Hutter, E.; Fendler, J. H.; Roy, D. *J. Phys. Chem. B* **2001**, *105*, 11159.
(21) Lyon, L. A.; Musick, M. D.; Natan, M. J. *Anal. Chem.* **1998**, *70*, 5177.
(22) Lyon, L. A.; Pena, D. J.; Natan, M. J. *J. Phys. Chem. B* **1999**, *103*, 5826.
(23) Hutter, E.; Pileni, M.-P. *J. Phys. Chem. B* **2002**, *107*, 6497.
(24) Ito, M.; Nakamura, F.; Baba, A.; Tamada, K.; Ushijima, H.; Lau, K. H. A.; Manna, A.; Knoll, W. *J. Phys. Chem. C* **2007**, *111*, 11653.
(25) Nakamura, F.; Ito, M.; Manna, A.; Tamada, K.; Hara, M.; Knoll, W. *Jpn. J. Appl. Phys.* **2006**, *45*, 1026.
(26) Jen, Y.-J.; F-Chiang, S.-H.; Liu, F.-K. *Jpn. J. Appl. Phys.* **2006**, *45*, 1850.
(27) He, L.; Smith, E. A.; Natan, M. J.; Keating, C. D. *J. Phys. Chem. B* **2004**, *108*, 10973.
(28) Chen, S.-J.; Chien, F. C.; Lin, G. Y.; Lee, K. C. *Opt. Lett.* **2004**, *29*, 1390.
(29) Wu, B.; Wang, Q. *Chin. Opt. Lett.* **2008**, *6*, 323.
(30) Rueda, A.; Stemmler, M.; Bauer, R.; Fogel, Y.; Mullen, K.; Kreiter, M. *J. Phys. Chem. C* **2008**, *12*, 14801.
(31) Yamaguchi, T.; Yoshida, S.; Kinbara, A. *J. Opt. Soc. Am.* **1974**, *64*, 1563.
(32) Carlan, A.; Desrousseaux, G. *J. Opt. Soc. Am.* **1978**, *68*, 1019.
(33) Yamaguchi, T.; Takahashi, H.; Sudoh, A. *J. Opt. Soc. Am.* **1978**, *68*, 1039.
(34) Yamaguchi, T.; Yoshida, S.; Kinbara, A. *Thin Solid Films* **1973**, *18*, 63.
(35) Yamaguchi, T.; Yoshida, S.; Kinbara, A. *Thin Solid Films* **1974**, *21*, 173.
(36) Aravind, P. K.; Metiu, H. *Surf. Sci.* **1983**, *124*, 506.
(37) Ruppin, R. *Surf. Sci.* **1983**, *127*, 108.
(38) Wind, M. M.; Vlieger, J.; Bedeaux, D. *Physica A* **1987**, *141*, 33.
(39) Uchiho, Y.; Kajikawa, K. *Chem. Phys. Lett.* **2009**, *478*, 211.
(40) Johnson, P. B.; Christy, R. W. *Phys. Rev. B* **1972**, *6*, 4370.
(41) Bagchi, A.; Barrera, R. G.; Fuchs, R. *Phys. Rev. B* **1982**, *25*, 7086.
(42) Bagchi, A.; Barrera, R. G. *Phys. Rev. Lett.* **1980**, *44*, 1475.
(43) Ui, H.; Tomioka, A.; Nishiwaki, T.; Miyano, K. *J. Chem. Phys.* **1994**, *101*, 6430.
(44) Topping, J. *Proc. Soc. Ser. A London* **1927**, *114*, 67.
(45) Bethune, D. S. *J. Opt. Soc. Am. B* **1989**, *6*, 910.

JP910438Q

日消誌　2010；107：1426―1433

今月のテーマ●B型肝炎ウイルス再活性化の問題点とその対策

B型肝炎再活性化による劇症肝炎の現状と対策

桶谷　眞　坪内博仁[1)]

要旨：近年，強力な免疫抑制・化学療法の普及によりB型肝炎ウイルスの再増殖によるHBV再活性化肝炎が増加している．また，従来から知られている非活動性キャリアからの再活性化に加え，既往感染者からの再活性化の報告が増え，*de novo* B型肝炎とよばれている．*de novo* B型肝炎は劇症化率が高く，劇症化例の予後は極めて不良である．HBV再活性化対策では免疫抑制・化学療法前にHBVキャリアだけでなく，既往感染者をスクリーニングすることが重要である．前者は治療開始前に，後者は治療中または治療終了後にHBV DNAが陽転化した時点で速やかに核酸アナログ製剤を使用する必要がある．

索引用語：HBV再活性化，*de novo* B型肝炎，劇症肝炎，リツキシマブ，核酸アナログ製剤

はじめに

肝機能正常の非活動性B型肝炎ウイルス（HBV）キャリアにおいて，自然経過もしくは免疫抑制剤の使用が誘因となり，HBVの再増殖により肝炎が発症することがあり，HBV再活性化（reactivation）と呼ばれる．HBV再活性化はHBV DNAの上昇とそれに引き続く急激なALTの上昇が特徴である[1)2)]．最近は化学療法や移植医療の進歩により，多様な抗癌剤や免疫抑制剤を使用する機会が増え，HBVが再活性化する事例が増加している．また，HBs抗原が陰性化した既往感染者からの再活性化もみられるようになり，*de novo* B型肝炎と呼ばれ，注目されている．

HBV再活性化は重症化しやすく肝不全に至ることがあるだけでなく，現疾患に対する治療の中断により予後に重大な影響を与える．本稿では*de novo* B型肝炎を含むHBV再活性化の病態とそれによる劇症肝炎の現状と対策について述べる．

I　非活動性HBVキャリアにおける再活性化

1．HBV再活性化の機序

HBV再活性化の多くは血液悪性腫瘍や固形癌にステロイドを含む抗癌剤やリツキシマブを使用した場合[3)4)]，自己免疫性疾患にステロイドやインフリキシマブを使用した場合など[5)6)]，宿主の免疫機能の低下を契機に発症する．また，HIV感染症[7)]，肝臓移植をはじめとする臓器移植後や骨髄移植後などでもみられる[8)~11)]．

HBVは母子感染や幼児期の水平感染でキャリア化し，免疫寛容期を経て思春期に肝炎期に入り，HBe抗原/HBe抗体のセロコンバージョンとともに，HBV DNA量が減少し，肝炎のない非活動性キャリア期に移行する．このような非活動性のキャリアではHBV DNA量10^4copies/ml未満の微量なウイルス増殖がみられるが，最近のリアルタイムPCR法など高感度の測定系で，その検出が可能となった．HBV DNA量の低下は，

1）鹿児島大学大学院消化器疾患・生活習慣病学

Current status and prevention of fulminant hepatitis due to hepatitis B reactivation

Makoto OKETANI and Hirohito TSUBOUCHI[1)]

1）Digestive Disease and Life-style Related Disease, Kagoshima University Graduate School of Medical and Dental Sciences

Corresponding author：桶谷　眞（oketani@m2.kufm.kagoshima-u.ac.jp）

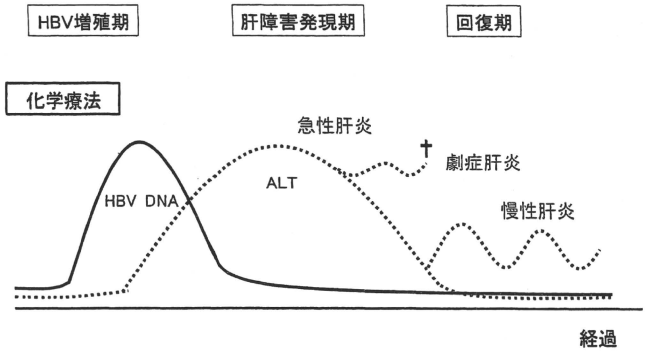

Figure 1. HBV再活性化の臨床経過.

ウイルス自体の増殖能の低下によるものとは限らず，宿主の免疫学的圧力によりもたらされたものである．したがって抗癌剤や免疫抑制剤により，この防御機構が破たんするとHBVは容易に増殖を開始する．

一般にHBV再活性化は ①HBVの増殖 ②肝障害の出現 ③回復の3段階からなる（Figure 1）．HBVの増殖は必ず肝障害の出現に先行し，その間には時間的ずれ（range 1〜11週）がある．まず，薬剤による免疫細胞の消失あるいは機能低下により，HBVが再増殖し感染細胞が拡大する．免疫機能が低下したままでは肝炎はおこりにくいが，薬剤の中止によりCTL（細胞障害性Tリンパ球）を中心とする免疫系が再構築された際には，短期間に感染細胞が広範に破壊され，重症肝炎が惹起される．感染細胞が排除され，免疫学的均衡が回復すると再び肝炎は鎮静化するが，慢性肝炎に移行することもあり，時に肝炎は致死的になる．

2. HBV再活性化の実態

HBV再活性化は，宿主の免疫機能，治療による免疫抑制の程度およびHBVの感染状態により影響される．HBV再活性化の危険因子として，男性，若年，ステロイド治療などが報告されているが[12]，治療前のHBV DNA量が多いことが最も重要な因子である[13]．ステロイド（グルココルチコイド）を使用するレジメンではHBV再活性化のリスクが増加するが，これはHBVゲノム内にglucocorticoid responsive elementがあり，ステロイドが直接的にウイルスを増殖させるためと考えられている[14]．悪性リンパ腫に対するシクロフォスファミド，ドキソルビシン，ビンクリスチン，プレドニゾロンを使用する化学療法では，HBs抗原陽性者の48%が再活性化し，7.4%に肝不全が惹起されたと報告されている[12]．HBe抗体陽性キャリアではpre C変異，BCP変異を持つウイルスが再活性化する可能性があり，肝炎を発症すると劇症化しやすいため注意が必要である[15][16]．

HBs抗原陽性キャリアに対する免疫抑制・化学療法の際には，従来より治療前に核酸アナログの予防投与が推奨されている．Lauらは30名のHBs抗原陽性の悪性リンパ腫患者に化学療法を施行する際にラミブジンの予防投与群と非投与群に分け比較試験を行った[17]．非投与群の53%にHBV再活性化がみられたのに対し投与群では1例もHBV再活性化はみられず，ラミブジン予防投与の有用性が検証された．

II HBV既往感染者における再活性化 —*de novo* B型肝炎

1. 既往感染者のHBVマーカー

成人でHBVに初感染すると急性肝炎がおこるが，通常は1〜3カ月の経過で肝炎は沈静化する．肝炎の回復期ではHBs抗原は陰性化し，HBs抗体が陽転化する．またHBc抗体は感染1カ月後

より陽転化し，長期間陽性のままである．このようなHBs抗原陰性で，HBc抗体ないしはHBs抗体が陽性の状態は既往感染と診断される．またHBVキャリアの感染晩期にも同様な状態がみられる．HBVの既往感染者はわが国では約20%存在すると推測されている．

これまでHBV既往感染者は，ウイルスが排除され，臨床的には治癒の状態と考えられてきた．しかし既往感染例においてもHBVはcccDNA（covalentlt closed circular DNA）として肝細胞核内に存在し，HBV DNAの複製が長期間持続していることが明らかになった[18][19]．このようなHBc抗体ないしHBs抗体が陽性の既往感染者において，免疫能の低下により惹起されるHBV再活性化を*de novo* B型肝炎と呼んでいる[20][21]．肝臓移植では，HBs抗原陰性かつHBc抗体陽性の肝臓を移植したレシピエントの33%から78%にHBV感染がみられる[8][9]．また，血液疾患における同種骨髄移植においても*de novo* B型肝炎は約50%と比較的高率に報告されている[10][11]．HBs抗原陰性であるが，血液中あるいは肝臓中にHBV DNAが少量検出される状態はOccult HBV infection（潜伏性HBV感染）と呼ばれるが，これらの多くはHBc抗体ないしはHBs抗体が陽性である[20]．

2. 既往感染者からのHBV再活性化

従来より化学療法後のHBV再活性化の中でHBs抗原陰性例の一部においても少数ながらHBV再活性化がおこることが知られていた[12]．しかし近年，強力な免疫抑制・化学療法を契機にHBs抗原陰性かつHBc抗体ないしHBs抗体陽性例からのHBV再活性化，すなわち*de novo* B型肝炎例が増加している[21][22]．*de novo* B型肝炎は特に悪性リンパ腫患者にリツキシマブとステロイドを併用した場合に高率にみられる．リツキシマブによる*de novo* B型肝炎は2001年にdervitéらにより最初に報告された[4]．その後，HuiらはHBs抗原陰性の悪性リンパ腫244例を対象に，前向きコホートで*de novo* B型肝炎の発症率を検討した．それによると*de novo* B型肝炎の発症頻度は，リツキシマブとステロイド併用化学療法では12.2%（6/49例）であったのに対し，併用していない場合では1.0%（2/195例）であり，リツキシマブとステロイド併用が*de novo* B型肝炎発症のリスク因子であった[23]．リツキシマブは抗ヒトCD20ヒト・マウスキメラ抗体からなるモノクローナル抗体で，CD20を発現する正常および腫瘍性B細胞を減少させる．これにより，液性免疫能の低下の他に抗原特異的CTLを誘導するB細胞の抗原提示機能も障害されると考えられる．リツキシマブ投与中には顕著にHBs抗体の低下が見られることからも，B細胞系に対する免疫抑制がHBV再活性化の誘因になっているものと思われる．

3. *De novo* B型肝炎の臨床像

De novo B型肝炎の臨床的特徴は，以下のとおりである．①化学療法終了後，HBV DNAの上昇がおこる（中央値12週）②HBV DNAの上昇から中央値10週でHBs抗原が陽転化し，その後中央値9.5週で肝炎が発症する（Figure 2）[22]．すなわち，HBV DNA上昇から肝炎発症までに中央値18.5週の時間的ずれがみられる．厚生労働省研究班では，過去5年間のB型急性肝炎1184例と*de novo* B型肝炎55例の全国調査結果を報告している[23]．それによると*de novo* B型肝炎は急性B型肝炎と比べ，発症年齢が高く，トランスアミナーゼのピーク値は900IU/Lと低いものの総ビリルビン値，HBV DNA量は有意に高値であった．劇症化率は*de novo* B型肝炎27%に対し急性肝炎で7%であり，また劇症化例の死亡率も*de novo* B型肝炎100%に対し急性肝炎44%と，いずれも*de novo* B型肝炎が有意に高率であった．劇症化した*de novo* B型肝炎5例はいずれもリツキシマブとステロイド併用の化学療法によるものあった．

III HBV再活性化による劇症肝炎の実態

厚生労働省研究班による劇症肝炎の全国調査では，HBV再活性化肝炎がB型例に占める割合は，2004年の8%（2/26例）から2008年は35%（8/23例）と増加している．さらにHBV再活性化肝炎のうち，発症前のHBs抗原陰性のいわゆる*de novo* B型肝炎と推測される症例は48%（14/